

Surface BRDF estimation from an aircraft compared to MODIS and ground estimates at the Southern Great Plains site

Kirk D. Knobelspiesse,¹ Brian Cairns,^{1,2} Beat Schmid,³ Miguel O. Román,⁴ and Crystal B. Schaaf⁴

Received 4 March 2008; revised 10 July 2008; accepted 12 August 2008; published 21 October 2008.

[1] Surface albedo, which quantifies the amount of solar radiation reflected by the ground, is an important component of climate models. However, it can be highly heterogeneous, so obtaining adequate measurements are challenging. Global measurements require orbital observations, such as those provided by the Moderate Resolution Imaging Spectroradiometer (MODIS). Satellites estimate the surface bidirectional reflectance distribution function (BRDF), a surface inherent optical property, by correcting observed radiances for atmospheric effects and accumulating measurements at many viewing and solar geometries. The BRDF is then used to estimate albedo, an apparent optical property utilized by climate models. Satellite observations are often validated with ground radiometer measurements. However, spatial and temporal sampling differences mean that direct comparisons are subject to substantial uncertainties. We attempt to bridge the resolution gap using an airborne radiometer, the Research Scanning Polarimeter (RSP). RSP was flown at low altitude in the vicinity of the Department of Energy's Southern Great Plains Central Facility (SGP CF) in Oklahoma during the Aerosol Lidar Validation Experiment (ALIVE) in September, 2005. The RSP's scanning radiometers estimate the BRDF in seconds, rather than days required by MODIS, and utilize the Ames Airborne Tracking Sunphotometer (AATS-14) for atmospheric correction. Our comparison indicates that surface albedo estimates from RSP and MODIS agree with Best Estimate Radiation Flux (BEFLUX) ground radiometer observations at the SGP CF. Since the RSP is an airborne prototype of the Aerosol Polarimetry Sensor (APS), due to be launched into orbit in 2009, these techniques could form the basis for routine BRDF validation.

Citation: Knobelspiesse, K. D., B. Cairns, B. Schmid, M. O. Román, and C. B. Schaaf (2008), Surface BRDF estimation from an aircraft compared to MODIS and ground estimates at the Southern Great Plains site, *J. Geophys. Res.*, *113*, D20105, doi:10.1029/2008JD010062.

1. Introduction

[2] A proper understanding of surface albedo has been a priority of the remote sensing community since its origins. Besides providing information about the nature of the surface itself, remote-sensing retrievals of atmospheric properties must often account for the effects of the surface reflectance. Albedo is also an important determinant of where radiation is absorbed in climate models, yet it is spatially and temporally heterogeneous, and thus difficult to

include realistically in those models. In addition, anthropogenic surface albedo changes can alter the global climate, but quantification of this process is dependent upon the data that are used by models [Myhre and Myhre, 2003]. Global albedo estimates from sensors on satellite platforms are now being compiled into climatologies appropriate for modeling [Lucht *et al.*, 2000b; Schaaf *et al.*, 2002; Luo *et al.*, 2005]. It is important, then, to verify the validity and accuracy of these global albedo products, and to identify any features of these products that would improve the reality of global models without introducing unnecessary complexity.

[3] Albedo is complex and highly variable. It is a function of the surface material and its topography, which is spatially and temporally heterogeneous, and the angle at which the surface is illuminated and observed. Low earth orbit satellite platforms with instruments such as the Moderate-Resolution Imaging Spectrometer (MODIS) and the Multi-angle Imaging SpectroRadiometer (MISR), as well as instruments on geostationary satellites [Martonchik *et al.*,

¹Department of Applied Physics and Applied Mathematics, Columbia University, New York, New York, USA.

²NASA Goddard Institute for Space Studies, New York, New York, USA.

³Atmospheric Science and Global Change Division, Pacific Northwest National Laboratory, Richland, Washington, USA.

⁴Department of Geography and Environment, Center for Remote Sensing, Boston University, Boston, Massachusetts, USA.

2002; Pinty *et al.*, 2005] are well suited to building climatologies for modeling purposes, as they have a spatial coverage and measurement repeat cycle that is impossible to achieve from ground or aircraft measurements. However, significant analysis is required to reduce the apparent optical properties (AOP's), as seen at a satellite, to inherent optical properties (IOP's) suitable for use in a climate model. Surface AOP's depend on the solar and viewing geometry and on the atmospheric state through extinction of the direct solar beam before and after it reaches the surface and scattering of radiation on its way to and from the surface. For example, the measurement that is closest to a direct estimate of albedo is the ratio of upwelling and downwelling fluxes, which is nonetheless an AOP since it depends on the atmospheric state. Since the atmospheric state varies within a climate model, the albedo must be described in an independent manner as an IOP of the surface, that is then used in a coupled calculation of the radiative transfer in the surface-atmosphere system. The bidirectional reflectance distribution function (BRDF) is an IOP that describes the reflectance of a surface when illuminated by an infinitesimally narrow beam of radiation and viewed through an equally infinitesimally narrow beam, and is a function of the geometry of those two beams. Because of this, the BRDF is a theoretical property that can only be estimated [Schaepman-Strub *et al.*, 2006]. Although several approaches have been developed for the estimation of the BRDF over a wide angular range [Bruegge *et al.*, 2000; Gatebe *et al.*, 2003] a more common BRDF estimation approach is to fit an atmospherically corrected and geometrically variable set of measurements to semi-empirical BRDF models [Engelsen *et al.*, 1998; Lucht *et al.*, 2000b]. The semi-empirical BRDF model can then be used to derive quantities that are not readily observable, such as the variation of the albedo as a function of solar zenith angle that is the function of relevance to most current climate models.

[4] BRDF estimation from orbit is subject to several hurdles. First, atmospheric effects must be removed, which is complicated by multiple surface-atmosphere interactions. Second, a sufficient angular range of measurements must be accumulated to provide a robust estimate of the semi-empirical BRDF model. In the case of fixed angle instruments such as MODIS, this accumulation requires several days, over which albedo characteristics may have changed. Multi-angle instruments such as MISR and the Research Scanning Polarimeter (RSP, described below) sample a much larger angular range nearly instantly, but this is at the expense of spatial coverage. Third, in order to be effective for global evaluation of albedo, the semi-empirical BRDF models must encompass a sufficient range of surface BRDF's that their marginal integrals, such as albedo, are not biased by the choice of model. Finally the data-model fitting method should be resistant to noise and methodological errors.

[5] Because of the difficulties of BRDF estimation from orbit, a robust validation effort is required to have sufficient confidence to apply satellite derived climatologies to climate models. As we noted above, ground radiometers make a measurement that is more directly related to albedo than remote sensing measurements and they make that measurement as the solar zenith angle varies over the course of the day. Correctly modeling this energy input to the surface as a function of solar zenith angle is important for general

circulation models. These measurements therefore provide the appropriate validation of the albedo derived from satellite, or aircraft measurements. However, care needs to be taken when comparing with the ground radiometers to properly account for the atmospheric state and the spectral sampling provided by the remote sensing measurements as compared to the total fluxes measured at the surface.

[6] Recently, there have been several efforts to compare MODIS albedo products to ground radiometer data from the Department of Energy's (DOE) Southern Great Plains Central Facility (SGP CF) in North-Central Oklahoma, USA [Luo *et al.*, 2003; Yang, 2006; Schaaf *et al.*, 2006], and to other ground radiometers [Liang *et al.*, 2002; Jin *et al.*, 2003]. For example, Yang [2006], compared parameterizations of MODIS albedo [Liang *et al.*, 2005; Wang *et al.*, 2007] to Best Estimate Radiation Flux (BEFLUX) radiometers [Shi and Long, 2002] and found some differences in the shape of the albedo as a function of solar zenith angle. Since the the BEFLUX radiometers provide the direct estimate of the energy input to the surface that we are interested in for global applications it is important to understand whether these differences were due to inadequacies in the MODIS data itself, its parameterizations, or problems with the comparison method.

[7] Albedo data measured from aircraft utilizing multi-angle and multi-spectral radiometers at the SGP CF offer the possibility to investigate and resolve this issue. The Aerosol Lidar Validation Experiment (ALIVE) was in September of 2005 in the vicinity of the SGP CF in northern Oklahoma. During ALIVE, a Jetstream-31 (J-31) turboprop aircraft flew several low altitude transects about 200 m above the SGP CF. The J-31 carried several instruments. The principal instrument used here is the Research Scanning Polarimeter (RSP), a scanning polarimeter that is intended for aerosol and cloud research and is a prototype for the Aerosol Polarimetry Sensor (APS). The APS is due to be launched as part of the NASA Glory mission in 2008 [Mishchenko *et al.*, 2007b]. RSP was flown at low altitudes to collect data for the best possible estimate of the surface reflectance and BRDF. More details about the RSP are given in section 2.3.1. The Ames Airborne Tracking Sunphotometer (AATS-14) was also on the J-31. The AATS-14 is a fourteen spectral channel sun tracking sun-photometer [Schmid *et al.*, 2006] that provides accurate measurements of aerosol optical depth above the aircraft. The AATS-14 measurements of aerosol above the aircraft in conjunction with measurements from AErosol RObotic NETwork (AERONET) [Holben *et al.*, 1998] ground-based sun-photometers allows us to perform an extremely accurate atmospheric correction of the RSP measurements. The atmospherically corrected RSP surface measurements were fit to BRDF models from which albedos were derived and compared to MODIS and BEFLUX results. In addition, a land cover based approach, similar to that used in Liang *et al.* [2002], was used to evaluate the differences in spatial scale between MODIS, RSP and BEFLUX data.

[8] The purpose of this paper is to evaluate the MODIS BRDF retrievals that use semi-empirical kernel models to derive albedos and surface albedo parameterizations. As part of this evaluation, we also investigate previous validation efforts at the SGP CF. RSP data provide a unique opportunity to bridge the spatial and temporal resolution

differences between MODIS and ground radiometers in a well characterized atmospheric regime at the SGP CF.

2. Background

2.1. Albedo, BRDF, and Other Definitions

[9] Instruments observe many forms of what we call reflectance, which can have a somewhat complicated and ambiguous terminology. We use nomenclature of *Nicodemus et al.* [1977], reviewed in *Schaepman-Strub et al.* [2006], which is briefly described here.

[10] Reflectance, as it is most generally described, is the ratio of radiant exitance from a surface to the irradiance, E , incident upon that surface. Both radiant exitance and irradiance have units of $[W m^{-2}]$, so reflectance, ρ , is unitless, and is constrained to the interval $[0, 1]$. The reflectance factor, R , is the ratio of the radiant exitance from a surface to the radiant exitance leaving a perfectly reflective, Lambertian (isotropic) surface under the same irradiance. Occasionally, such as the case of strong forward reflectance, the reflectance factor can exceed one. Both are functions of solar zenith angle, θ_s , view zenith angle, θ_v , solar azimuth angle, ϕ_s , view azimuth angle ϕ_v , and wavelength, λ . We define wavelength for the narrow band instruments of interest here (RSP and MODIS) as the solar spectrum weighted center, Λ , of the spectral band of a particular instrument.

[11] The bidirectional reflectance distribution function (*BRDF*) describes the scattering of a parallel beam of incident light from one direction into another direction, defined as the ratio of the radiance observed through an infinitesimally small solid angle cone to the irradiance illuminating that surface within an infinitesimal solid angle.

$$BRDF(\theta_s, \theta_v, \phi_s, \phi_v, \lambda) = \frac{dL(\theta_s, \theta_v, \phi_s, \phi_v, \lambda)}{dE(\theta_s, \phi, \lambda)} [sr^{-1}] \quad (1)$$

[12] The radiance, L , is the quantity of radiant flux per unit solid angle per unit wavelength and has units of $[W m^{-2} sr^{-1}]$. The *BRDF* is an inherent optical property (IOP) and thus represents the intrinsic properties of the surface. Since it is defined with infinitesimal quantities it can not be directly measured. Its estimation, however, is important since apparent optical properties (AOP's) can be derived from the *BRDF* in a consistent fashion appropriate for validation. Moreover, given the typical scale of angular *BRDF* variations, it can be sampled and accurately estimated.

[13] *Schaepman-Strub et al.* [2006] cites several AOP's that can be derived from the *BRDF*, but we use only two. The directional-hemispherical reflectance (*DHR*), called the “black-sky” albedo in MODIS terminology, is the view geometry integrated, total radiant exitance when the surface is irradiated by a plane parallel beam. This is also known as the planetary albedo in the astronomical literature.

$$DHR(\theta_s, \phi_s, \lambda) = \int_0^{2\pi} \int_0^{\frac{\pi}{2}} BRDF(\theta_s, \theta_v, \phi_s, \phi_v, \lambda) \cos(\theta_v) \cdot \sin(\theta_v) d\theta_v d\phi_v \quad (2)$$

[14] Many publications assume *DHR* is independent of the solar azimuth angle (ϕ_s) which is the case if the *BRDF* only depends on the difference between view and solar azimuth angles. If surface properties have no preferred direction this is a reasonable assumption. In our case in central Oklahoma, many of the surfaces are plowed fields or otherwise human influenced, so the *DHR* will not necessarily be invariant with respect to solar azimuth angle and the *BRDF* will depend on both the view and solar azimuth angles independently. The magnitude of this azimuth angle dependence is unknown. To maintain consistency with previous literature and MODIS and BEFLUX products, we assume solar azimuth angle independence, but comment further on this issue in section 4.5.

[15] Another albedo related quantity is the bihemispherical reflectance (*BHR*), which represents the solar and view geometry integration of the *BRDF* (or the solar geometry integration of the *DHR*). When the solar downwelling is assumed isotropic, *BHR* is the “white-sky” albedo in MODIS terminology. This is also known as the spherical albedo in the astronomical literature.

$$BHR(\lambda) = \int_0^{\frac{\pi}{2}} \int_0^{2\pi} \int_0^{\frac{\pi}{2}} \int_0^{2\pi} BRDF(\theta_s, \theta_v, \phi_s, \phi_v, \lambda) \cdot \cos(\theta_v) \sin(\theta_v) \cos(\theta_s) \sin(\theta_s) d\theta_v d\phi_v d\theta_s d\phi_s \quad (3)$$

[16] A function that we will define is the normalized *DHR* (*nDHR*). Many climate models assume that the shape of the *DHR* is spectrally invariant, and thus take as inputs that shape and some scaling factor as a function of wavelength and surface type. The *nDHR* is defined to be

$$nDHR(\theta_s) = \frac{DHR(\theta_s, \lambda)}{DHR(60^\circ, \lambda)} \quad (4)$$

[17] The *nDHR* will be used to compare different albedo related measurements and to provide a direct comparison with the previous work of *Yang* [2006].

2.2. Ross-Li BRDF Kernel Models

[18] The *BRDF* is a theoretical parameter impossible to measure directly, even with the large number of view angles available with the RSP. *BRDF* estimation is aided with the use of surface reflectance models, where available measurements are fit with a combination of kernels, each representing the geometric reflectance behavior a particular surface type. In this work, we use the kernel models employed in MODIS *BRDF* products, as described in *Lucht et al.* [2000b], and hereafter referred to as the Ross-Li *BRDF* model. Previous work has identified these kernels as providing a robust and efficient framework for *BRDF* estimation [*Schaaf et al.*, 2002] on a global scale, even when only a limited geometric range of measurements are available. Our assessment of the use of these particular kernels here is therefore limited to how well they represent the dense angular sampling of the RSP measurements. An assessment of the *BRDF* model validity for use in the evaluation of the surface albedo in global climate models is provided by comparisons to BEFLUX data.

[19] The Ross-Li BRDF model decomposes surface reflectance into three types of scattering, and combines them in the following form:

$$\begin{aligned} BRDF(\theta_s, \theta_v, \phi, \lambda) &\simeq R(\theta_s, \theta_v, \phi, \lambda) \\ &= f_{iso}(\lambda) + f_{vol}(\lambda)K_{vol}(\theta_s, \theta_v, \phi) \\ &\quad + f_{geo}(\lambda)K_{geo}(\theta_s, \theta_v, \phi) \end{aligned} \quad (5)$$

where K_{vol} and K_{geo} are the volumetric and geometric scattering kernels, respectively, and f_{iso} , f_{vol} and f_{geo} , are the isotropic, volumetric and geometric kernel scaling parameters. ϕ is the relative view-sun azimuth angle ($\phi = \phi_v - \phi_s$). In practice, an optimization is used to find the best kernel scaling parameters (f) to a set of measured reflectances (R). The result is an estimation of the BRDF.

[20] The first scaling parameter, f_{iso} , represents isotropic scattering, which has no dependence on incidence or view angle and thus does not have a geometrically dependent kernel. Volumetric scattering represents the scattering within a dense vegetation canopy, and is based on a radiative transfer approximation of single scattering due to small, uniformly distributed and non-absorbing leaves. The angular behavior of this kernel is to have a minimum near the backscatter direction and bright limbs. As described in *Roujean et al.* [1992] and *Ross* [1981], the volumetric kernel, normalized to zero for $\theta_v = \theta_s = 0$, is:

$$K_{vol} = \frac{(\pi/2 - \xi) \cos \xi + \sin \xi}{\cos \theta_s + \cos \theta_v} - \frac{\pi}{4} \quad (6)$$

where ξ is the scattering angle, defined to be $\cos \xi = \cos \theta_v \cos \theta_s + \sin \theta_v \sin \theta_s \cos \phi$.

[21] Geometric scattering represents surfaces with larger gaps between objects, and thus accounts for self shadowing. The angular behavior of this kernel is therefore to have a maximum at backscattering where there are no shadows. K_{geo} is based on the work of *Wanner et al.* [1995] and *Li and Strahler* [1992], but is used in the reciprocal form given in [*Lucht et al.*, 2000a]. This reciprocal form, in the special case that the ratio of the height of the tree at the center of the crown to the vertical crown radius (h/b in *Luo et al.* [2005]) is two and the ratio of the vertical crown radius to the horizontal crown radius is one (spherical, or compact crowns, b/r in *Luo et al.* [2005]) as is used in the MODIS data processing, is

$$\begin{aligned} K_{geo} &= O(\theta_s, \theta_v, \phi) - \sec \theta_s - \sec \theta_v + \frac{1}{2}(1 + \cos \xi) \sec \theta_s \sec \theta_v \\ O &= \frac{1}{\pi} (t - \sin t \cos t) (\sec \theta_s + \sec \theta_v) \\ \cos t &= \frac{\sqrt{D^2 + (\tan \theta_s \tan \theta_v \sin \phi)^2}}{\sec \theta_s + \sec \theta_v} \\ D &= \sqrt{\tan^2 \theta_s + \tan^2 \theta_v - 2 \tan \theta_s \tan \theta_v \cos \phi} \end{aligned} \quad (7)$$

2.3. Instrument Description

2.3.1. RSP

[22] The Research Scanning Polarimeter is an airborne prototype for the Aerosol Polarimetry Sensor (APS), due to be launched in 2008 as part of the NASA Glory Project

[*Mishchenko et al.*, 2007b]. The main goals of RSP/APS are to retrieve a complete suite of aerosol and cloud microphysical parameters together with the vertical distribution and integrated number concentration of particles from orbit [*Mishchenko et al.*, 2004, 2007a]. The RSP has nine optical channels with center wavelengths of 410, 470, 555, 670, 865, 960, 1590, 1880 and 2250 nm. This work utilizes all of these bands except for the 960 and 1880 nm channels, which are used to estimate water vapor column amounts and detect thin cirrus clouds respectively. Details about the RSP/APS aerosol retrieval using polarimetry can be found in *Cairns* [2003] and *Chowdhary et al.* [2002].

[23] In addition to measuring the polarized reflectance beneath the RSP with each scan, the instrument also measures the total (unpolarized) reflectance. While this information is not currently utilized to retrieve aerosol parameters over land, it is useful to independently validate surface albedo values retrieved by MODIS or other orbital platforms. Each RSP scan begins about 60° forward of nadir in the direction of aircraft motion, and samples at 0.8° intervals to about 60° aft of nadir. Thus each scan contains about 150 instantaneous samples at a variety of sensor viewing geometries. A BRDF estimation is therefore possible with a larger set of surface anisotropic reflectances, as opposed to fixed viewing angle instruments, such as MODIS, which require an accumulation of observations over several days (16 in case of the MODIS MCD43B product) before the BRDF can be estimated [*Lucht et al.*, 2000b]. The instantaneous field of view (IFOV) of the RSP is fourteen milliradians, which corresponds to a 2.8 m ground pixel size assuming an altitude of 200m above the ground. RSP measurements were made over a period of two weeks during the ALIVE campaign in September, 2005. Two flights, labeled JRF03 and JRF04 in ALIVE terminology, were on September 16th and were chosen for this analysis for the clear, cloudless conditions at that time, and the low altitude segments of those flights that were made in the vicinity of the SGP CF. More details about data selection for the RSP are in section 3.1.1.

[24] The RSP performed two types of flights during ALIVE. The first type was to collect data at an altitude above the majority of the atmospheric aerosols, generally 4–5 km above ground on September 16th, 2005. An indication of the required altitude was provided by the AATS-14, see section 2.3.2. The atmospheric state is determined from these measurements, which are then applied in the atmospheric correction of data from the second type of measurements, collected at as low an altitude as possible. These low altitude data (about 200 m above the ground) were used for BRDF estimation. The low altitude was key to minimize the atmospheric effect between the RSP and the ground, maximize spatial resolution, and minimize the effect of aircraft motion on efforts to combine views from different scans into a multi-angle observation of a single surface location.

2.3.2. AATS-14, Ancillary Data, and the Radiative Transfer Model

[25] RSP surface reflectance retrievals utilized several types of ancillary data. These data were used in the atmospheric correction of the observed radiances to remove atmospheric effects. An important component of the RSP atmospheric correction was the Ames Airborne Tracking

Sunphotometer (AATS-14), co-located on the J-31 with the RSP. The AATS-14 provides a continuous record of aerosol optical depth above the aircraft in fourteen channels from 354 to 2139 nm [Schmid *et al.*, 2006]. These data were used in three ways. First, AATS-14 measured the vertical extent and distribution of aerosols during aircraft ascent and descent. This identified the required altitude for “high altitude” RSP measurements where aerosol parameters are retrieved. Second, information about the aerosols, such as the nature of their vertical distribution and the presence of very large coarse mode aerosols helped constrain the RSP aerosol retrievals. Finally, AATS-14 measurements during “low altitude” flights identified where in the aerosol layer the aircraft was located. This is particularly useful when AATS-14 data are compared to AERONET ground sunphotometers, which thus indicates the aerosol optical depth between the instrument and the ground.

[26] Several other sources of data provide ancillary information necessary to remove the effect of various components of the atmosphere. Ozone absorption, which is greatest in the 470 and 555 nm bands, is based on the daily $1^\circ \times 1^\circ$ values from the Total Ozone Mapping Spectrometer (TOMS) [McPeters and Center, 1998]. Absorption due to NO_2 , greatest at the shortest wavelength channels, is estimated using Scanning Imaging Absorption Spectrometer for Atmospheric Chartography (SCIAMACHY) data [Bovensmann *et al.*, 1999]. Water vapor content was measured by the Microwave Radiometer (MWR) located at the SGP CF [Morris, 2006].

2.3.3. MODIS

[27] The MODerate resolution Imaging SpectroRadiometer (MODIS) is a multispectral remote sensing satellite in a polar orbit. There are actually two MODIS instruments, on the morning equator crossing NASA Terra (EOS-AM) and afternoon equator crossing NASA Aqua (EOS-PM) spacecraft. Terra was launched in 1999, and Aqua in 2002. Since ALIVE was in September of 2005, we used a combination of data from both instruments. MODIS produces a large number of atmospheric and surface products, but we have focused our attention on the surface albedo retrievals, referred to as product ID MCD43 in MODIS terminology. We used the “collection five” processing version, which has a 500 m ground resolution. MODIS measures surface reflectance at a single view zenith angle with each scan, so albedos are determined by fitting several days worth of data (containing a variety of view and solar zenith angles) to a set of BRDF models (described in section 2.2). The methodology for doing so is described in Lucht *et al.* [2000b] and Strahler *et al.* [1999], and first operational results are presented in Schaaf *et al.* [2002].

[28] A number of efforts have been made to validate MODIS albedo products. Often, this takes the form of a comparison of satellite MODIS results to measurements from ground based radiometers. However, care must be taken to ensure that this comparison accounts for the spatial and temporal resolution differences between remote sensing instruments and ground radiometers. MODIS (and RSP) measurements represent a combination of all reflectances within a pixel, which may include a variety of surface types, while ground radiometers measure albedo with a smaller spatial scale that is dependent on the height of the tower on which the upwelling flux measurement is made and the

observed portion of the radiative spectrum. In addition, the multi-day data aggregation required with the MODIS dataset could be problematic if that aggregation period includes changes to surface properties. It is therefore difficult to determine if comparisons represent purely instrumental differences, or are also affected by resolution.

[29] Prior to the launch of Terra, Lucht *et al.* [2000a] attempted to validate the BRDF kernel fitting method by comparing ground radiometer measurements to reflectances from other remote sensing platforms. Spatial resolution differences were controlled by doing this comparison in a region of low albedo variability (grass and scrubland in New Mexico, USA), and BHR results were close enough for accurate climate modeling. Liang *et al.* [2002] validated MODIS albedo by “upsampling” ground radiometer measurements from an agricultural region in Maryland, USA. They report less than 5% absolute error. Jin *et al.* [2003] compared MODIS albedo to field measurements from the Surface Radiation Budget Network (SURFRAD) and found results that met an accuracy requirement of 0.02 for measurements between April and September. Winter measurements failed to meet requirements, most likely due to the influence of rapid albedo changes from snow. With the launch of Aqua, Salomon *et al.* [2006] updated MODIS albedo validation for the combined Terra/Aqua product using SURFRAD and radiometers at the SGP CF. He found that, while wintertime albedo remain uncertain as described in Jin *et al.* [2003], overall coverage improved while total data averages remained consistent with previous results.

[30] Validation efforts described above are generally restricted to comparisons of BHR, whereas for climate modeling a DHR parameterization is also needed. Several attempts have been made to parameterize MODIS results for application in climate models. Liang *et al.* [2005] created a parameterization using DHR and BHR from MODIS, soil moisture from the North American and Global Land Data Assimilation System (LDAS), fractional vegetation cover, and leaf and stem area index. Wang *et al.* [2007] used a simplification of MODIS DHR and a measure of vegetation type to create another type of parameterization. Yang [2006] investigated the validity of these parameterizations of DHR by comparing them to BEFLUX radiometer values at the SGP CF. While both parameterizations agreed well with each other at this site, Yang [2006] found differences in comparison to ground radiometers. Parameterization values were much smaller than BEFLUX values at high solar zenith angles and larger than BEFLUX values at very small solar zenith angles. While the former is perhaps to be expected considering the lack of MODIS data at high solar zenith angles, the latter is unexpected and troubling. Our work was initiated as an attempt to further investigate and possibly resolve the differences found in Yang [2006] with regards to how well MODIS surface albedo data products can predict surface albedo.

2.3.4. BEFLUX

[31] Ground radiometer data were supplied by the Best Estimate Flux (BEFLUX) value-added procedure (VAP), which is created from several radiometers at the Department of Energy’s Atmospheric Radiation Measurement (ARM) Southern Great Plains Central Facility (SGP CF). BEFLUX radiometers measure diffuse and total hemispherical downwelling irradiance and total hemispherical upwelling

Table 1. Low Altitude ALIVE Flight Segments Used for Surface Characterization

	JRF3	JRF4
Date	09/16/2005	09/16/2005
Start time, UTC	16:32:25	22:09:32
Number of RSP scans	270	41
J-31 Altitude above sea level	510 m	475 m
Relative sensor-solar azimuth	-45°	156°
Solar zenith angle	43°	62°
AERONET $\tau_a(\lambda = 500 \text{ nm})$	0.07	0.05
AATS-14 $\tau_a(\lambda = 499 \text{ nm})$	0.06	0.05
sky conditions	clear	clear

irradiance in one minute intervals [Shi and Long, 2002]. These values were combined according to the methodology of Yang [2006] to compute a *BHR* and *DHR* representing the rural pasture at the SGP CF in North-central Oklahoma, USA. This was done in two steps. First, the *BHR* for the entire month of September, 2007 was determined by finding the average ratio of total upwelling to total downwelling irradiance from cloudy measurements. These cloudy measurements were identified by the ratio of direct to total hemispherical downwelling irradiance. The *BHR* was then utilized to find the *DHR* on the day of the measurement.

3. Method

3.1. RSP Data Preparation

3.1.1. Data Selection

[32] The Aerosol Lidar Validation Experiment (ALIVE) was a field campaign performed in North-central Oklahoma in September of 2005. This is the location of the Southern Great Plains Central Facility (SGP CF) of the Atmospheric Radiation Measurement (ARM) Program (Department of Energy). While the primary goals of the ALIVE campaign were not to investigate RSP surface characterization, the proximity to the suite of ground based instruments at the SGP site, simultaneous measurements of the aerosol profile from AATS-14, and a series of low altitude flights, provide an ideal data-set with which to investigate the surface characterization.

[33] Several short, low altitude flight segments were made in the vicinity of the SGP site, typically preceded or followed by a spiral maneuver used by the AATS-14 to determine an aerosol optical thickness altitude profile. Surface characteristics were typical for the rural mid-west of the United States in the fall. The ground was relatively flat, and covered by a patchwork of late-season crops, bare soil exposed by recent harvesting, and mixtures of trees and shrubs [Luo et al., 2003]. There are few buildings and the occasional paved road.

[34] Data from two flights were used. Table 1 presents these flight times, along with geometry, aerosol and weather conditions. Aerosol optical thickness at 500nm from an AERONET Project [Holben et al., 1998] sun photometer at the SGP site is also included to provide an understanding of aerosol properties from that day.

[35] In Table 1, the tags in the first row (JRFx) identify the research flight. Start time for a data file within that flight is listed in UTC. Local time was five hours earlier. Scans were selected from a particular data file so that they

included only low altitude, constant heading segments. Altitude is listed as meters above sea level. Ground height at the SGP site is about 315 m, so flights had an above ground height between 160 and 195 m. The (relative) azimuth is the instrument heading minus solar azimuth, in degrees. Aerosol optical thickness at 500 nm (τ_a) was measured by the AERONET Project with a ground sun photometer at the SGP site. Values from the time of flight are provided for comparison. AATS-14 optical thickness was measured on the J-31. Thus differences between AATS-14 and AERONET represent the optical thickness between the aircraft and the ground, a value which is well within the AERONET and AATS-14 uncertainty. The last row contains a visual description of the cloud scenario from the instrument operator.

[36] There were a total of twelve research flights as part of ALIVE, but only flights JRF3 and JRF4, listed above, were suitable for BRDF estimation. JRF3 and JRF4 were the only flights with low altitude segments when the sky was completely devoid of clouds. As we shall see later (see section 3.1.3), some effort was put into determining the diffuse downwelling irradiance while estimating the BRDF. This determination is only accurate, with our models, for clear skies. Including the effects of clouds under partially cloudy skies, even if implemented with a three dimensional radiative transfer code, would introduce large uncertainties, as there is limited information to specify the vertical and horizontal cloud distribution.

3.1.2. Classification and Mixed Pixel Removal

[37] Before the Ross-Li BRDF models were fit to the data, we separated it into similar classes, and performed our fitting on each class individually. This was done to limit the dependence on data coverage differences from flight to flight, and also to facilitate comparisons with other lower spatial resolution data sets. Prior to image classification, gaseous absorption effects were removed as described above, and a metric describing the amount of vegetation (a vegetation index, see Appendix B) was calculated for each data point. Data were then split into “soil” and “vegetation” classes and extreme vegetation index values were removed. Boundary or mixed surfaces were also removed using an edge detection convolution kernel on the spatial image of vegetation index. In addition, analyses were performed on an “all” class which contains the entire data-set except for data that were removed as part of the quality control process. For each of these classes the data were then fit with the Ross-Li BRDF model.

[38] Simple thresholding of the Aerosol Resistant Vegetation Index (ARVI, see Appendix B for details on how it is computed) was used to split the data into a “soil” and “vegetation” class. ARVI values between -0.25 and 0.075 were classified as “soil”, while ARVI values between 0.375 and 0.775 were classified as “vegetation”. Such narrow ARVI regions centered on the modes of each surface type were chosen to avoid mixed pixel data and focus on the properties of generic “soil” and “vegetation”. Figure 1 is a histogram of the ARVI for each flight. Peaks for both classes are pronounced, and vertical dashed lines show the regions used for each class. The histogram computed using different small segments of the view angle range (not pictured here) is similar to the one shown here indicating an absence of significant BRDF effects on this index. Each

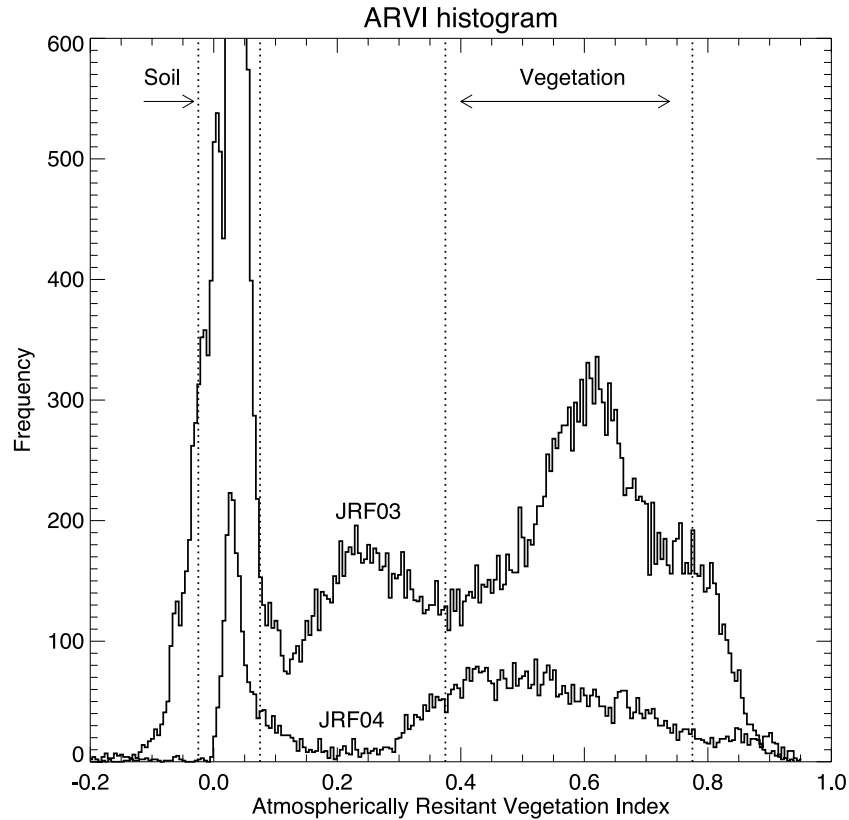


Figure 1. Histograms of the Atmospherically Resistant Vegetation Index (ARVI) for each flight. Vertical dotted lines represent the boundaries of the “soil” and “vegetation” class thresholds.

flight flew over slightly different areas in the region of the SGP CF, so there are some differences between the histograms of each flight. In particular, JRF03 has a third peak at about an ARVI of 0.25, possibly indicating post-harvest, sparsely vegetated, fields that were not observed during JRF04. Since that surface type is not present in JRF04 data, it was omitted in the study. Furthermore, JRF04 contains less data than JRF03, as the length of flight time dedicated to the low altitude segment was less in JRF04. Few measurements passed the “soil” class criteria. After additional screening, described below, only the “vegetation” class remained from JRF04. Finally, a third, “all” class was created for ARVI values between -0.25 and 0.775 . For consistency, additional screening procedures described below were applied to this class as well.

[39] To further restrict our data to generic land types, the ARVI spatial image is used to identify data that is in the middle of a patch of soil or vegetation. An edge detection algorithm was applied that uses a discrete convolution with a 3×3 spatial kernel. This kernel is applied as a multiplier to each pixel and its neighbors in the image, and the summed result of each multiplication forms the value of that pixel in the resulting image. This is a discrete version of the gradient and the technique (when this mask is added to the original image to enhance boundaries) is also called unsharp masking [Gonzalez and Woods, 1992]. The gradient image is used to remove boundary and mixed pixels. A threshold, $\eta = 0.1$, was chosen such that pixels satisfying $|\nabla(\text{ARVI})| > \eta$ are excluded. η was selected arbitrarily, but it is of the same magnitude as the ARVI range for the soil

class, thus adjacent pixels containing as much variability as the narrowest class (or more) are removed. Figure 2 illustrates the classification and imagery from flight JRF3. Classification results (in part 2d) compare favorably with intuition from the imagery (part 2a), and take boundary and edge pixels (part 2c) into account. Note also the small quantity of data available for analysis. For safety reasons, the aircraft was flown at low altitude for only short segments near the SGP site.

[40] Several geometric screening criteria were also applied. Data with view zenith angles greater than 65° were removed. This was done to avoid view angles at the extremes of measurement capability. Since the RSP is scanning in the direction of aircraft motion, data from turns were excluded because those scans may not represent a single ground location. Thus, data from aircraft headings 3° greater or less than an average heading were removed. The effects of both of these geometric screening criteria are evident in Figure 2d, where data at the right of the image have been removed because their zenith angle was too large, and data at the top removed because this is where the aircraft began banking into its spiral ascent for the next segment of the flight.

[41] Image data were rearranged so that each scan represents a set of view angles about a single ground location, rather than the actual order of measurements (which represent a set of view angles about an airborne location). While this has no effect on the actual data, classification results for each scan were checked for consistency. This final screening criteria (which is not displayed in Figure 2) required that

JRF03 imagery, vegetation index, index variability, and classification results

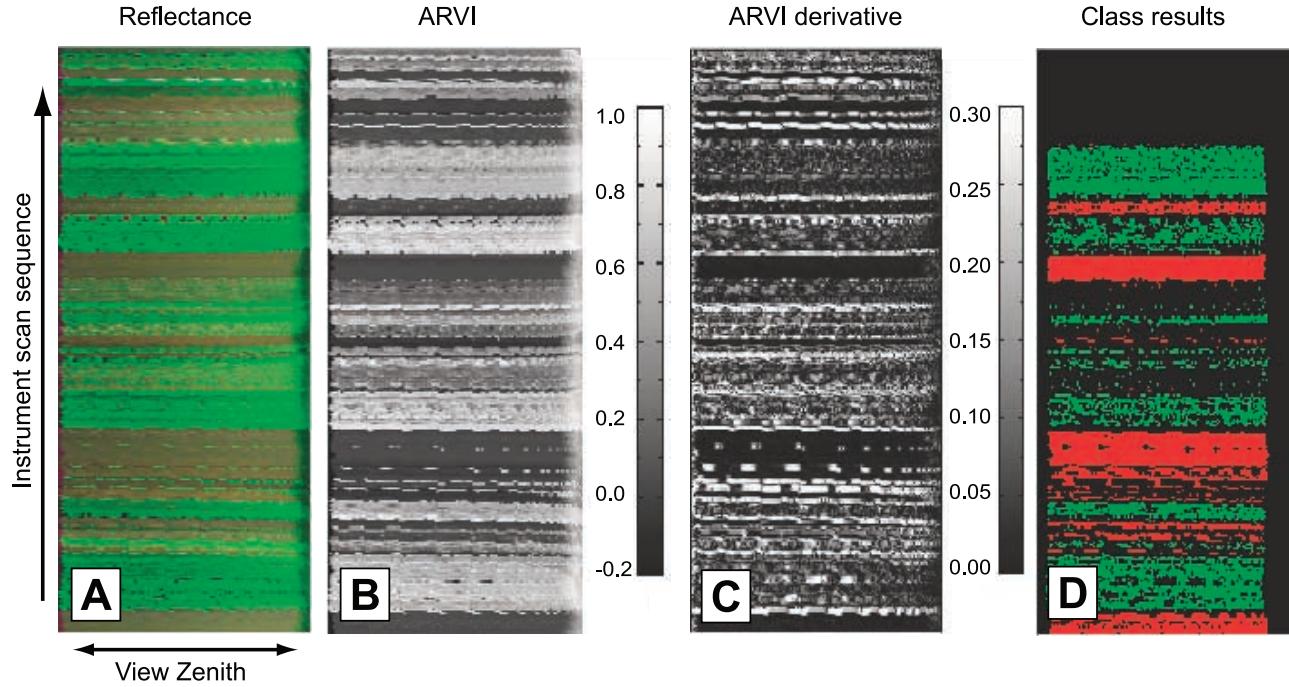


Figure 2. Data from flight JRF03 was used to show (from left to right), (a) Ground reflectance, where the 670 nm band is displayed in the red channel, the 865 nm band in the green channel, and the 470 nm band in the blue channel, (b) Atmospherically Resistant Vegetation Index (ARVI), with the color bar at the right, (c) gradient of ARVI, used to remove boundary and edge pixels with its color bar at the right, and (d) classification results, where red indicates “soil” type, green indicates “vegetation”, and black are unclassified areas.

50% of the data in a scan must have passed all previous screening criteria and were grouped into a single class. The result is a set of data that is of a consistent surface type over most of the view angle range and that has had any outlier measurements, which may represent noise, surface boundary or mixed pixel effects removed.

3.1.3. Determination of Ground Reflectance and the Diffuse Effect

[42] Measurement of ground reflectance from an aircraft requires adequate compensation for atmospheric effects. During ALIVE, a high quality characterization of the atmospheric scattering was provided by the combination of polarized RSP measurements (above the aerosol layer) with the vertical profile of aerosol optical thicknesses from the AATS-14. This cannot be used to determine the ground reflectance directly because of the multiple scattering that occurs between the atmosphere and the surface. The atmospheric correction is therefore performed using an iterative process, where initial estimates of surface reflectance are adjusted until the surface-atmosphere scattering model reproduces the reflectance measured by the RSP.

[43] The atmospheric-surface model uses the doubling and adding method [Lacis and Hansen, 1974; Hansen and Travis, 1974], and produces a reflectance to compare to RSP data, given aerosol and other atmospheric properties together with solar and instrument geometry and kernel

values for the Ross-Li BRDF reflectance model. The observed reflectance can be separated into an atmospheric and a surface component:

$$\rho^o(\theta_s, \theta_v, \phi, \lambda) = \rho^a(\theta_s, \theta_v, \phi, \lambda) + S(\theta_s, \theta_v, \phi, \lambda) \quad (8)$$

where ρ^o is the reflectance at the altitude of the observations, ρ^a is the reflectance due to atmospheric scattering of radiance into the instrument field of view without interacting with the surface (path radiance) and S includes all surface interaction terms. In what follows we are primarily interested in S and the correction for diffuse and multiple interaction terms, since we have an accurate and comprehensive characterization of the atmosphere from high altitude RSP measurements that allows us to calculate ρ^a . We will differentiate between measurements and model calculations by using a caret for those quantities that are direct observations. The surface interaction term, S , can be calculated using the expression

$$\begin{aligned} S(\theta_s, \theta_v, \phi, \lambda) = & [t^\dagger(\theta_v, \lambda) + T^\dagger(\lambda)] \rho^g(\theta_s, \theta_v, \phi, \lambda) [t^\dagger(\theta_s, \lambda) + *T^\dagger(\lambda)] \\ & + [t^\dagger(\theta_v, \lambda) + T^\dagger(\lambda)] \Sigma(\theta_s, \theta_v, \phi, \lambda) \rho^g(\theta_s, \theta_v, \phi, \lambda) \\ & \cdot [t^\dagger(\theta_s, \lambda) + *T^\dagger(\lambda)] \end{aligned} \quad (9)$$

where ρ^g is the surface reflectance, t is the direct solar transmittance, and T is the diffuse transmittance, with the arrows indicating whether they apply to transmission from the sun to the ground (\downarrow) or from the ground to the observational altitude (\uparrow). The star symbol, $*$, indicates that integrations over zenith and azimuth are performed for diffuse interactions. As is usually the case for scattering problems with no preferred azimuthal plane, that integration is actually implemented using a Fourier decomposition and re-summation [Hovenier, 1971; Hansen and Travis, 1974; de Haan et al., 1987]. The function Σ is used in the calculation of multiple surface atmosphere interaction terms and is given by the formula

$$\Sigma(\theta_s, \theta_v, \phi, \lambda) = \sum_{i=1}^{\infty} (\rho^g(\theta_s, \theta_v, \phi, \lambda) * \rho^{a*}(\theta_s, \theta_v, \phi, \lambda))^i \quad (10)$$

where ρ^{a*} is the reflectance of the atmosphere illuminated from below. The implementation of this summation is described in [Hovenier, 1971; Hansen and Travis, 1974; de Haan et al., 1987].

[44] In equation (8), ρ^o is measured by the RSP and calculated with the doubling-adding model, while ρ^a , t , T and Σ are determined from the model based on the atmospheric state that is prescribed by AATS-14, AERONET and high altitude RSP data. The model includes the effects of both Rayleigh (molecular) and aerosol scattering. In order to find an estimate of ρ^g that has the effects of diffuse transmission and multiple surface-atmosphere scattering removed, we use the following iteration

$$\begin{aligned} \rho_{p+1}^g(\theta_s, \theta_v, \phi, \lambda) &= \left[\frac{\hat{S}(\theta_s, \theta_v, \phi, \lambda)}{S_p(\theta_s, \theta_v, \phi, \lambda)} \right] \rho_p^{g,k}(\theta_s, \theta_v, \phi, \lambda) \\ &= \gamma_p(\theta_s, \theta_v, \phi, \lambda) \rho_p^{g,k}(\theta_s, \theta_v, \phi, \lambda) \end{aligned} \quad (11)$$

where p is the iteration index, $\rho^{g,k}$ is the kernel fit to the latest estimate of surface reflectance and \hat{S} is the observation corrected for path radiance. We have implicitly defined the function γ_p , which is the ratio of measurement to model S , to adjust the surface reflectance until the model calculated reflectance matches the observations. This iteration is similar to that introduced by Chahine [1968] for atmospheric sounding. The kernel fit to the reflectance uses a least mean square estimate of the kernel coefficients, so the vector of kernel coefficients, \mathbf{f} , is given by the expression

$$\mathbf{f}_{p+1} = \left([\mathbf{K}(\theta_v)^T \mathbf{K}(\theta_v)]^{-1} \mathbf{K}(\theta_v)^T \right) \rho_{p+1}^g(\theta_v) \quad (12)$$

and the kernel estimate for the surface reflectance at the observed viewing geometry is

$$\rho_{p+1}^{g,k}(\theta_v) = \mathbf{K}(\theta_v) \mathbf{f}_{p+1} \quad (13)$$

with \mathbf{K} being the $3 \times N$ reflectance kernel matrix formed from the isotropic, volumetric and geometric kernels (cf. equation (5)) and N is the number of view angles for the given viewing geometry. \mathbf{K} and \mathbf{f} depend on the same set of wavelength (λ) and other geometric parameters (θ_s , ϕ), so

those subscripts are omitted from the above equations. The iteration is initialized with the value

$$\rho_1^g(\theta_s, \theta_v, \phi, \lambda) = \frac{\hat{S}(\theta_s, \theta_v, \phi, \lambda)}{t^\uparrow(\theta_v) t^\downarrow(\theta_s)} \quad (14)$$

[45] In an atmosphere with no scattering this initial value gives the atmospherically corrected surface reflectance, and no further iterations are therefore necessary. Otherwise, equations (11) through (13) are iterated until γ is close to unity. If there is scattering in the atmosphere, we can determine that $\gamma < 1$ from equation (9) for the first step in the iteration. This is a necessary condition for the convergence of this iteration [Twomey, 1977]. Convergence also requires that the matrix associated with the estimate of the kernel parameters is diagonally dominant [Dubovik and King [2000], Appendix C). Since we are interested in the convergence of the estimation of the weights associated with the kernels we define matrix \mathbf{M}

$$M_{jk} = \left(\frac{\partial \ln[\rho^{g,k}(\theta_{v,l})]}{\partial \ln[f_j]} \right)^{-1} \frac{\partial \ln[S(\theta_{v,l})]}{\partial \ln[f_k]} \quad (15)$$

where we use the convention that there is a summation over repeated subscripts. The average degree of diagonal dominance of that matrix, dd , is

$$dd = \sum_i \frac{\sum_{i \neq j} |M_{ij}|}{M_{ii}} \quad (16)$$

[46] As expected (see Figure 3), dd is largest at shortest wavelengths, where the effects of scattering are largest, and smallest at the longer wavelengths, where the effects of scattering are negligible.

[47] The final iteration products are the kernel values of the Ross-Li surface reflectance model. The iteration was repeated between 5–9 times for each band until the change in kernel values for each iteration was smaller than 10^{-5} .

3.1.4. Spectral to Broadband Albedo Computation

[48] *DHR* and *BHR*, as calculated in the previous section, represent surface properties in a set of narrow instrument bands. Data from these narrow bands must be spectrally interpolated if they are to be compared to broadband ground radiometer data such as that from BEFLUX. In MODIS products, this is done according to the methodology of Liang [2001] and validated in Liang et al. [2003]. Liang [2001] used libraries of surface reflectance spectra and model simulations to create a set of coefficients that are applied to scene albedo values to approximate a broadband *DHR* or *BHR*. These coefficients are applied uniformly across the entire MODIS dataset. Our RSP-ALIVE dataset comprises a single day with a well known atmospheric scenario. In this sense, we are fortunate in that we can utilize knowledge about the atmosphere in our broadband albedo computation, and we do so as follows.

[49] Conversion of *DHR*(Λ , θ_s) to the broadband version *DHR*_{bb}(θ_s) involves the spectral integration of the *DHR* weighted by the downwelling solar irradiance. Irradiances are computed using a hyperspectral version of the doubling and adding model applied in section 3.1.3 [Cairns et al.,

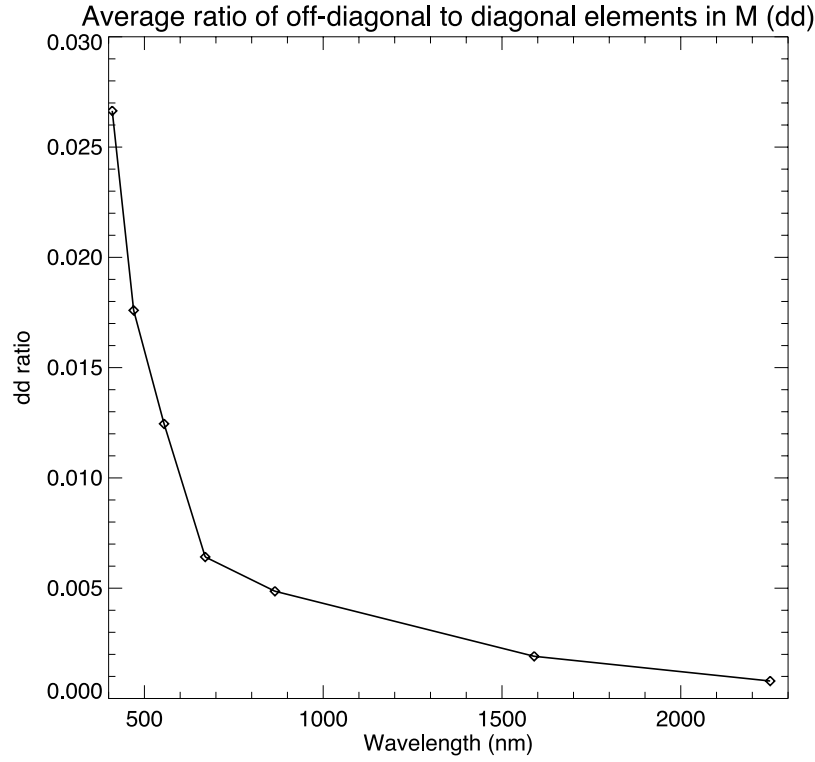


Figure 3. Average (for each wavelength band) ratio of off-diagonal to diagonal elements of matrix **M** (see equation (15)). This ratio, *dd*, is described in equation (16).

2003]. Spectral *DHR*'s are created using linear interpolations of Ross-Li kernel weights, f , determined in section 3.1.3. This is then normalized by the total downwelling solar irradiance appropriate for a particular day at all wavelengths

$$DHR_{bb}(\theta_s) = \frac{\int_{\lambda_{\min}}^{\lambda_{\max}} E_o(\lambda) t(\lambda) DHR(\lambda, \theta_s) d\lambda}{\int_{\lambda_{\min}}^{\lambda_{\max}} E_o(\lambda) t(\lambda) d\lambda} \quad (17)$$

where $E_o(\lambda)$ is the exo-atmospheric irradiance and $t(\lambda)$ is the direct solar transmittance. Spectrally dependent *DHR*(λ) is created by linear interpolation of kernel weights and application of the *DHR* parameterization described in *Lucht et al.* [2000b].

$$\begin{aligned} DHR(\lambda, \theta_s) = & f_{iso}(\lambda) + f_{vol}(\lambda)g_{0,vol}(\lambda) + f_{geo}(\lambda)g_{0,geo}(\lambda) \\ & + \theta^2 [f_{vol}(\lambda)g_{1,vol}(\lambda) + f_{geo}(\lambda)g_{1,geo}(\lambda)] \\ & + \theta^3 [f_{vol}(\lambda)g_{2,vol}(\lambda) + f_{geo}(\lambda)g_{2,geo}(\lambda)] \end{aligned} \quad (18)$$

g parameters from *Lucht et al.* [2000b] are in Table 2. *BHR*_{bb} is computed in a similar fashion, where spectrally interpolated kernel weights are applied to *Lucht et al.* [2000b]'s *BHR* parameterization. This parameterization is then integrated in a weighted manner.

$$BHR_{bb} = \frac{\int_{\lambda_{\min}}^{\lambda_{\max}} E_o(\lambda) t(\lambda) BHR(\lambda) d\lambda}{\int_{\lambda_{\min}}^{\lambda_{\max}} E_o(\lambda) t(\lambda) d\lambda} \quad (19)$$

$$BHR(\lambda) = f_{iso}(\lambda)w_{iso} + f_{vol}(\lambda)w_{vol}(\lambda) + f_{geo}(\lambda)w_{geo}(\lambda) \quad (20)$$

[50] For consistency, broadband *BHR*_{bb} and *DHR*_{bb} are computed using the same method for both RSP and MODIS, and are thus integrated over the same spectral range (400 nm to 2500 nm). It should be noted that this is not the same spectral range as the standard MODIS broadband albedo products, but it matches the range of BEFLUX radiometers. We also analyzed the radiative effect of albedo beyond this spectral range using the hyperspectral doubling and adding model from *Cairns et al.* [2003] and estimates of surface albedo by extrapolating the RSP “vegetation” and “soil” data from within the measured spectral range. We found that the relative error in estimation of *DHR* (of the entire radiative system) using our restricted spectral range was 3.0% for “vegetation” and 0.7% for the darker “soil” data. The absolute bias for a surface with an albedo of 0.2 is 0.0058 and 0.0014 for “vegetation” and “soil”, respectively. This estimation accounted for Rayleigh (molecular) scattering alone. Aerosols and absorbing gases would have the effect of further reducing the out of band radiance, and thus decreasing the above errors.

3.2. MODIS Data Preparation

[51] The newly reprocessed (Collection V005) MODIS BRDF/Albedo product is now being produced from Aqua

Table 2. *Lucht et al.* [2000b] *DHR* Parameters

	Isotropic	Volumetric	Geometric
g_0	1.0	−0.007574	−1.284909
g_1	0	−0.070987	−0.166314
g_2	0	0.307588	0.041840
w	1.0	0.189184	−1.377622

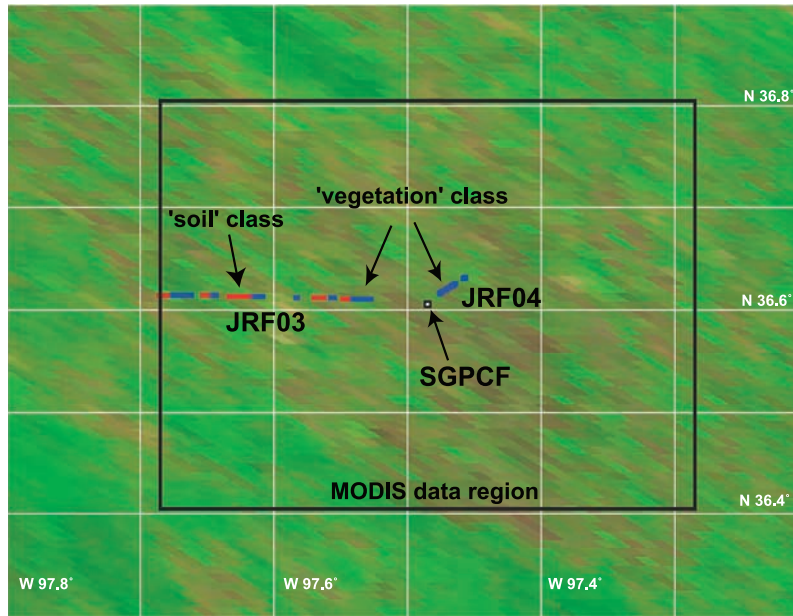


Figure 4. MODIS nadir reflectances from September 16th, 2005, overlaid with RSP data and SGP CF locations. MODIS data are a composite of reflectance from band 1 (645 nm) in the red channel, band 2 (859 nm) in the green channel, and band 3 (469 nm) in the red channel. Data were scaled to give an intuitive impression of vegetation or bare soil dominance in each pixel. The black box identifies the region of MODIS data utilized in this study. RSP flight data locations are indicated in blue (“vegetation” class) or red (“soil” class) for both JRF03 (left) and JRF04 (right). The SGP CF is indicated with the black and white square.

and Terra data every eight days at an increased 500-meter spatial resolution. The spectral product provides semi-empirical, kernel-driven anisotropy models which are retrieved from all clear-sky, high quality, atmospherically-corrected surface reflectances available over a 16-day period. This is done by fitting multiple observations to the Ross-Li BRDF kernel models, as described in section 2.2 and in *Lucht et al.* [2000b]. The resulting BRDF parameters (f_{iso} , f_{vol} and f_{geo}) are then used to compute integrated albedos for MODIS spectral bands 1–6 (centered at 0.648, 0.858, 0.470, 0.555, 1.240, and 1.640 μm respectively). Collection V005 MODIS/Terra+Aqua BRDF/Albedo products are Validated Stage 1, meaning that accuracy is estimated using a small number of independent measurements obtained from selected locations at particular times.

[52] MODIS data utilized in this study was taken from a $0.4^\circ \times 0.4^\circ$ box surrounding the SGP CF. This geographic area was selected to encompass both the SGP CF and RSP overflight locations. Direct pixel to pixel comparisons were not performed due to the vast differences in spatial (and temporal) resolution between the terrestrial BEFLUX, airborne RSP and orbital MODIS [*Liang et al.*, 2002]. Figure 4 shows the spatial context of the three data-sets. An attempt was made to identify “vegetation” and “soil” classes as was done in section 3.1.2 for the RSP data. However, since band spectral sensitivities and the spatial scale of MODIS and RSP are different, this is impossible to reproduce exactly. The NDVI was calculated (equation (B1)) for each pixel, where the MODIS $BHR(859 \text{ nm})$ was used in place of L_{NIR} and $BHR(645 \text{ nm})$ was used in place of L_{red} . The distribution of the result has a mean NDVI of about 0.5, with a normally distributed, half

maximum width of about 0.4. In an attempt to identify pixels that were “pure” with respect to ground surface type, those with NDVI values less than 0.3 were classified as “soil” pixels, while those with NDVI values greater than 0.7 were identified as “vegetation” pixels. Since these class types are not defined the same way as RSP classes and are of a different spatial scale, they cannot be definitively compared. However, this classification is representative of the spectral diversity present in the MODIS data.

3.3. BEFLUX Data Preparation

[53] BEFLUX ground radiometer data were prepared in the same manner as *Yang* [2006]. Irradiances measured by the BEFLUX radiometers are a combination of DHR_{bb} and BHR_{bb} , which must be separated prior to comparisons with MODIS or RSP data. This is done by measuring the albedo when the surface is illuminated diffusely (when it is cloudy), so the measured albedo is BHR_{bb} alone. The BHR_{bb} is then removed from the observations for cloud free days to compute the DHR_{bb} .

[54] The BEFLUX BHR_{bb} was calculated using data from the month of September, 2005. This length of time was chosen because it is long enough to have cloudy days for computation of BHR_{bb} , yet short enough that changes in surface properties can be ignored. Prior to BHR_{bb} calculation, data were screened to remove poor quality irradiances (as identified by Quality Control values), albedos greater than 0.4, and measurements made when the upwelling radiometers observed irradiances less than 10 W/m^2 (which is the instrument uncertainty). Measurements where the solar zenith angle was greater than 80° were removed as an additional screening that was not part of *Yang* [2006].

Table 3. Wang *et al.* [2007] Albedo Parameters

Vegetation type:	Type 10: Grassland	Type 12: Crop
$DHR(60^\circ, \Lambda_{VIS})$:	0.099	0.066
$DHR(60^\circ, \Lambda_{NIR})$:	0.295	0.286
B_1 :	0.57	0.62
B_2 :	0.12	0.13
$f_{geo}(\Lambda_{VIS})$:	0.056	0.041
$f_{vol}(\Lambda_{VIS})$:	0.012	0.009
$f_{geo}(\Lambda_{NIR})$:	0.168	0.177
$f_{vol}(\Lambda_{NIR})$:	0.035	0.037

Cloudy days were identified where the ratio of downwelling diffuse irradiance to total hemispheric downwelling irradiance was greater than 0.99. For September, 2005, 1901 measurements fit this criteria, which is just over 10% of the total number of measurements passing the initial screening criteria. The average BHR_{bb} from BEFLUX is 0.185, with a standard deviation of 0.012. BHR_{bb} was invariant for the month of September, 2005, as a linear fit with respect to time increases by only 0.002 during the month. As an aside, this helps confirm that the sixteen day period over which MODIS gathered measurements to form its BRDF estimate was free of temporal variability that could add to the error in these measurements, at least in the area immediately surrounding the BEFLUX radiometers. It should also be noted that the effective BHR observed by the BEFLUX radiometers under cloudy skies is not necessarily the same as that for clear skies. This is due to the different effective regions of influence that contribute to the measurements from multiple scattering between the surface and the atmosphere or cloud. Thus, although the spatial domain that contributes to the DHR estimated from BEFLUX is primarily determined by the height and location of the mount from which the downward looking measurements are made, the corrections used in equation (21) have a much more poorly defined spatial domain.

[55] DHR_{bb} is found by removing the effect of BHR_{bb} from the ratio of upwelling to downwelling irradiances in cloud-free conditions. Specifically, this uses the expression

$$DHR_{bb}(\theta_s) = \frac{U_{all}(\theta_s) - BHR_{bb}D_{diff}(\theta_s)}{D_{dir}(\theta_s)} \quad (21)$$

where $U_{all}(\theta_s)$ is the total hemispherical upwelling irradiance measured by the radiometer, $D_{dir}(\theta_s)$ is the direct downwelling irradiance, and $D_{diff}(\theta_s)$ is the diffuse downwelling irradiance. We performed this calculation for data from September 16th, 2005. Total Sky Imager (TSI) derived products [Long *et al.*, 2001] indicate that there were small (less than 10%) amounts of cloud cover during the morning and for part of the late afternoon. Data whose opaque cloud sky percentage was greater than 1% or whose thin cloud sky percentage was greater than 5% were removed. Unlike Yang [2006], we did not fit a polynomial to the computed DHR_{bb} , as we have a much smaller set of data and do not want to introduce fitting artifacts. The results were instead compared directly to MODIS, RSP and the parameterized MODIS data.

3.4. Albedo Parameterizations

[56] The final component of this multiple instrument comparison is a parameterization of MODIS albedos suitable for use in climate models. Wang *et al.* [2007] proposed a parameterization based only upon the MODIS reflectance factor at $\theta_s = 60^\circ$ and two vegetation type dependent parameters. This parameterization was also tested in Yang [2006]. The Wang *et al.* [2007] parameterization is motivated by the polynomial fit to the Ross-Li BRDF kernels presented in equation (46) of Lucht *et al.* [2000b], and has the following form (equation (7) in Wang *et al.* [2007])

$$DHR(\theta_s, \Lambda) = DHR(60^\circ, \Lambda) \cdot (1 + B_1(\Lambda)[g_1(\theta_s) - g_1(60^\circ)] + B_2(\Lambda)[g_2(\theta_s) - g_2(60^\circ)]) \quad (22)$$

[57] Here, g_1 and g_2 are the Ross-Li BRDF kernel polynomial fit coefficients from Table 1 in Lucht *et al.* [2000b], and B_1 and B_2 are the ratios of $f_{vol}/DHR(60^\circ, \Lambda)$ and $f_{geo}/DHR(60^\circ, \Lambda)$, respectively. Wang *et al.* [2007] used global MODIS measurements to determine median $DHR(60^\circ, \Lambda)$ and B values for about a dozen surface vegetation types. He did so using spectrally broad, visible (VIS) and Near-Infrared (NIR) spectral bands. We compared to the “Grassland” and “Cropland” vegetation types, as they are most consistent with the observed surface at the SGP CF. Table 3 lists parameter values for those vegetation types, along with the kernel values they imply.

4. Results

4.1. RSP Model Fitting Results

[58] The first, and most direct way of comparing $BRDF$ estimation results from RSP and MODIS is to examine the approximated $BRDF$ retrievals. As described in equation (1), $BRDF$ is a function of spectra (λ), solar and viewing zenith angles (θ_s and θ_v), and the relative azimuth angle ($\phi = \phi_v - \phi_s$, an assumption made in most literature). Because of the high dimensionality, we present a “slice” of the $BRDF$ estimated for the “all” surface class for RSP and MODIS in Figure 5. Generally speaking, the magnitude and $BRDF$ angular dependence for RSP and MODIS are similar. Largest differences are for the longest wavelength values, where the band locations for RSP and MODIS have the greatest dissimilarities. Better agreement in the visible bands could also be due to their use in the classification routines described previously, as divergent longer wavelength reflectances are not used to identify a class.

4.2. BHR (White-Sky Albedo)

[59] Figure 6 is a plot of the spectral and broadband BHR values for RSP and MODIS “all”, “soil” and “vegetation” classes. Spectral dependence is very similar to the magnitude of isotropic kernel values in Figure 5. BHR peaks are evident in the “vegetation” class in the green and NIR bands, while “soil” class BHR values are greatest at longer wavelengths. For “vegetation” and “soil” classes, RSP and

Figure 5. BRDF approximation results for MODIS (first and third rows) and RSP (second and fourth rows) during ALIVE. These results are for the ‘all’ surface type class with a solar zenith angle of 30° .

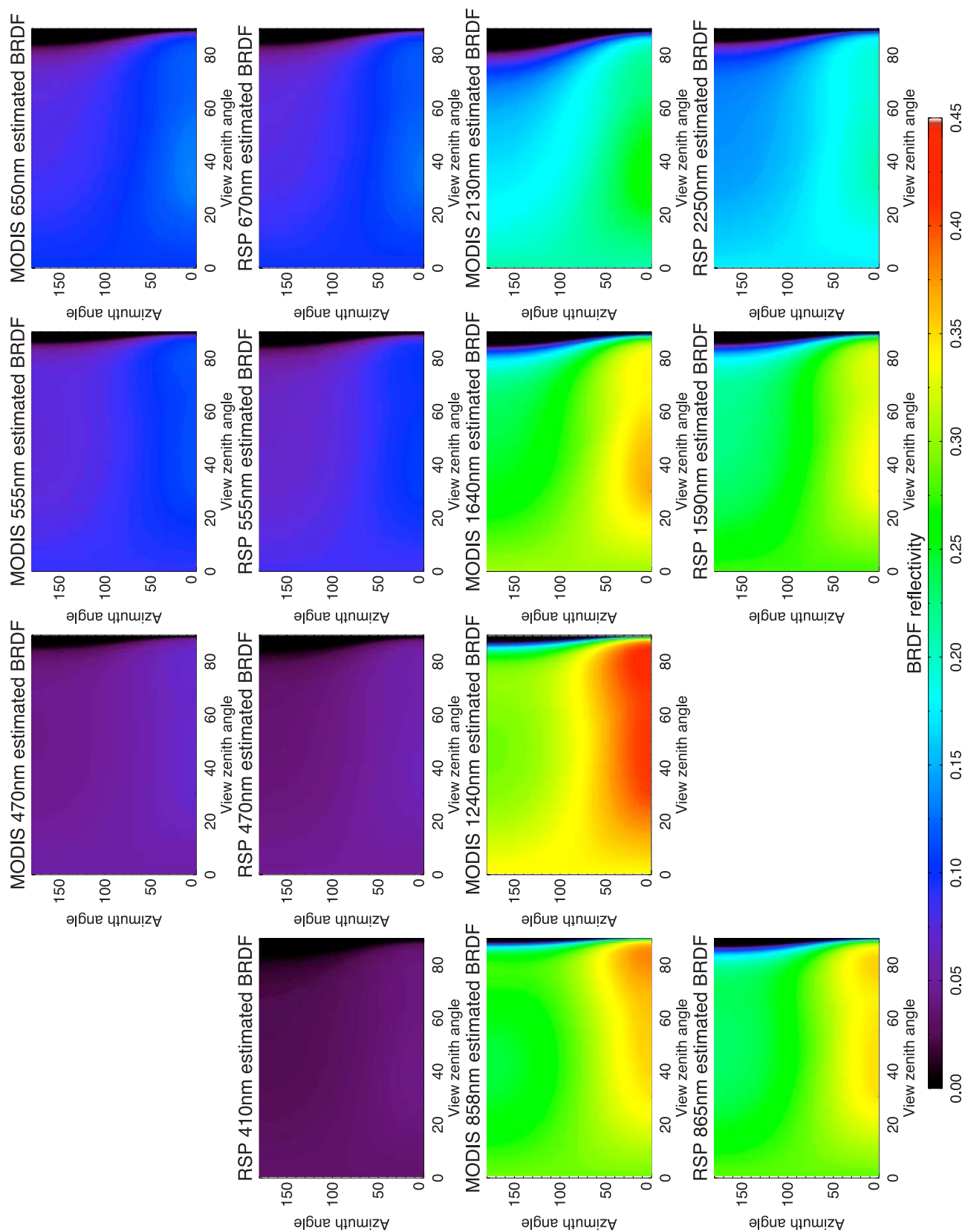


Figure 5

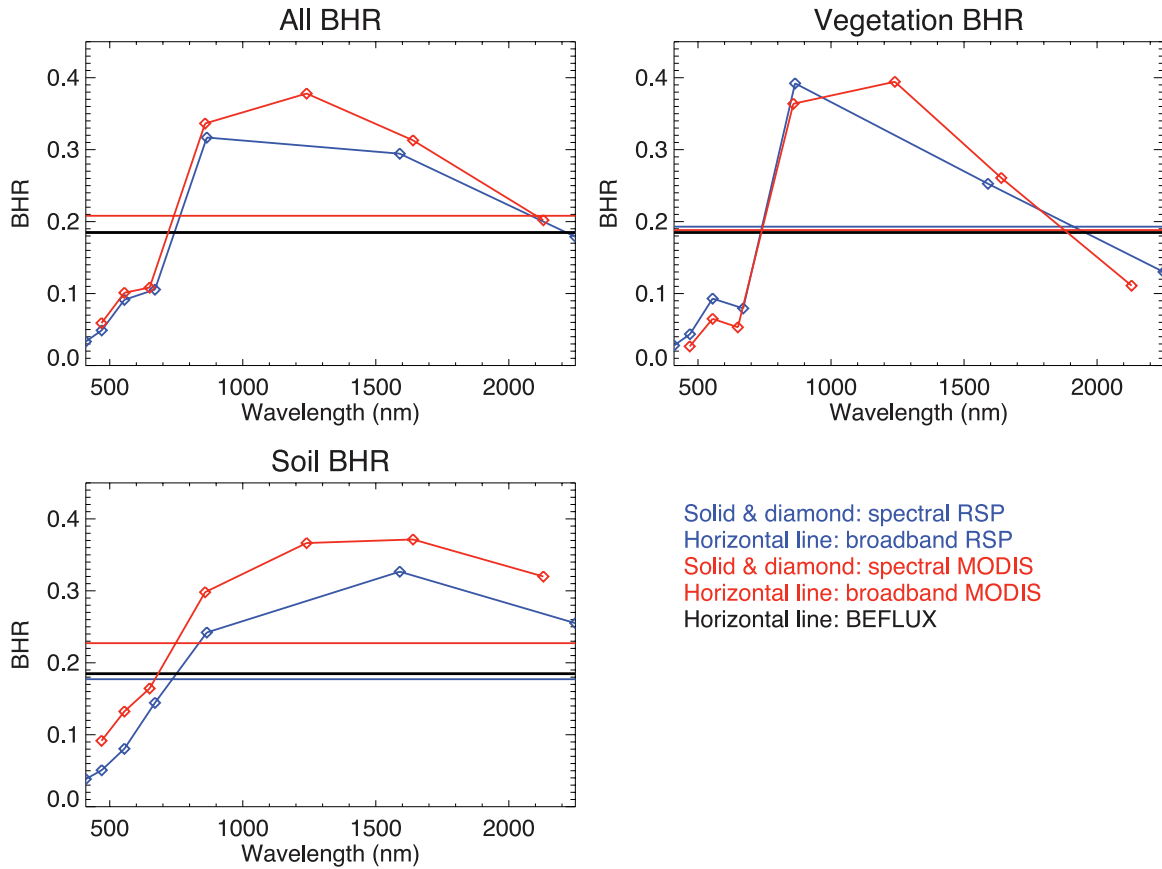


Figure 6. RSP (blue lines with diamonds) and MODIS (red lines with diamonds) $BHR(\lambda)$. “All” results are on the top left, “vegetation” class results on the top right, and “soil” class results on the bottom left. Straight horizontal lines represent the broadband BHR_{bb} , where again RSP is indicated in blue and MODIS in red. The thick black line is the BEFLUX BHR_{bb} .

MODIS BHR agree best in the visible wavelength bands that were used to classify the data, and generally agree within a BHR of 0.05 at other wavelengths. Broadband BHR comparisons show similar levels of agreement, with the difference between RSP and MODIS for the “all” class of 0.023. The RSP “all” BHR_{bb} is the closest match to the BEFLUX BHR , with a BHR_{bb} 0.0001 greater than that derived from BEFLUX. Interestingly, the best match of spectral BHR between RSP and MODIS are with the “all” classes, with similar spectral bands having differences less than 0.025. Although the “vegetation” and “soil” classes were derived with the intent of creating comparable RSP and MODIS albedos, the best agreement is for the average behavior of the two data sets. This is presumably because spatial averaging reduces the effects of the different spatial resolutions of the two sensors. Table 4 contains the tabulated BHR values displayed in Figure 6.

4.3. DHR (Black-Sky Albedo)

[60] Figure 7 is a plot of the DHR for each spectral band and the broadband DHR_{bb} . RSP vegetation and soil classes are plotted along with vegetation and soil from MODIS. As expected, DHR_{bb} roughly represents the mean magnitude and shape of the spectral DHR from which it is created. This is particularly true for longer wavelengths, which were more heavily weighted in the spectral to broadband conversion

due to a combination of higher exo-atmospheric irradiance, atmospheric transmittance, and surface reflectance. The shape and spectral variation of the DHR is similar for RSP and MODIS, as we would expect based on the similarity of the kernel values and the spectral BHR values presented in Figures 5 and 6.

[61] It is important to note that estimation of the BRDF using the kernel approach may be unphysical for angles other than those used to estimate the BRDF. Although the DHR calculated directly from the integrals of the BRDF kernels (as given by Lucht *et al.* [2000b]) remains physical (positive) for the kernel values analyzed here, the underlying BRDF may actually have negative values for high view or solar zenith angles. Great care should therefore be exercised in the use of these kernel estimated BRDF’s at such high (greater than 75°) angles.

[62] Model inputs require, among other things, the shape of DHR with respect to solar zenith angle. Yang [2006] expresses this shape by normalizing DHR by its value at $\theta_s = 60^\circ$. Figure 8 shows those normalized DHR ($nDHR$) values for both broadband and spectral values from the “vegetation” and “soil” classes of RSP and MODIS. Here, the broadband $nDHR$ is most similar to the longer wavelength visible or NIR $nDHR$. This illustrates the significance of those bands in forming broadband DHR .

Table 4. *BHR* From RSP, MODIS and the Wang *et al.* [2007] Parameterizations^a

	RSP-A	RSP-V	RSP-S	MOD-A	MOD-V	MOD-S	Wang-G	Wang-C
410 nm	0.033	0.028	0.038					
470 nm	0.049	0.044	0.051	0.059	0.027	0.092		
555 nm	0.091	0.093	0.081	0.101	0.065	0.132		
650 nm				0.108	0.053	0.164		
670 nm	0.106	0.079	0.144					
858 nm				0.336	0.364	0.298		
865 nm	0.317	0.392	0.242					
1240 nm				0.378	0.394	0.366		
1590 nm	0.294	0.253	0.327					
1640 nm				0.313	0.261	0.371		
2130 nm				0.202	0.111	0.320		
2250 nm	0.179	0.130	0.255					
Visible				0.086	0.045	0.126	0.095	0.068
NIR				0.317	0.319	0.314	0.282	0.271
BB	0.185	0.193	0.177	0.208	0.188	0.227		
Diff	0.000	0.008	−0.008	0.023	0.003	0.042		

^aRSP “all”, “vegetation” and “soil” classes are indicated RSP-A, RSP-V and RSP-S, respectively. Likewise, MODIS “all”, “vegetation” and “soil” classes are indicated MOD-A, MOD-V and MOD-S. Wang *et al.* [2007] “grassland” and “cropland” visible and NIR *BHR* values are indicated by Wang-G and Wang-C. The final row is the difference between the column *BHR_{bb}* and the BEFLUX derived *BHR_{bb}* = 0.185.

4.4. Remote Sensing, Ground Radiometer and Parameterization Comparison

[63] Perhaps the most important results of this work, Figure 9, is a comparison of *DHR* estimates from all RSP and MODIS classes to those derived from BEFLUX ground radiometers and parameterizations from two surface classes

of Wang *et al.* [2007]. BEFLUX data represent individual measurements on September 16, 2005, where any potentially cloud contaminated values are removed. Despite the thorough cloud screening, measurements at the same solar zenith angle (between 33° and 55°) are different for the morning and afternoon. This variability expresses the mag-

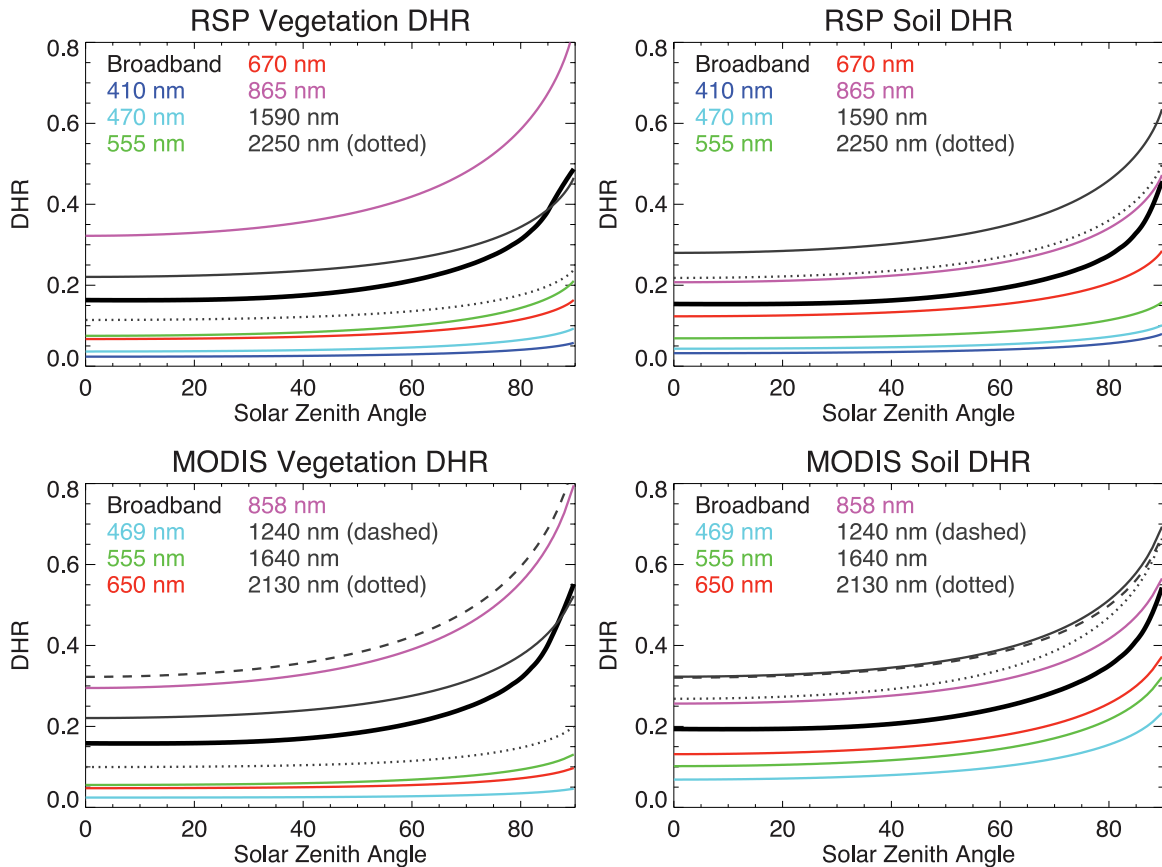


Figure 7. RSP (top) and MODIS (bottom) *DHR*(Λ, θ_s) values. “Vegetation” results are on the left, “soil” class results on the right. *DHR_{bb}(θ_s)* is indicated in black.

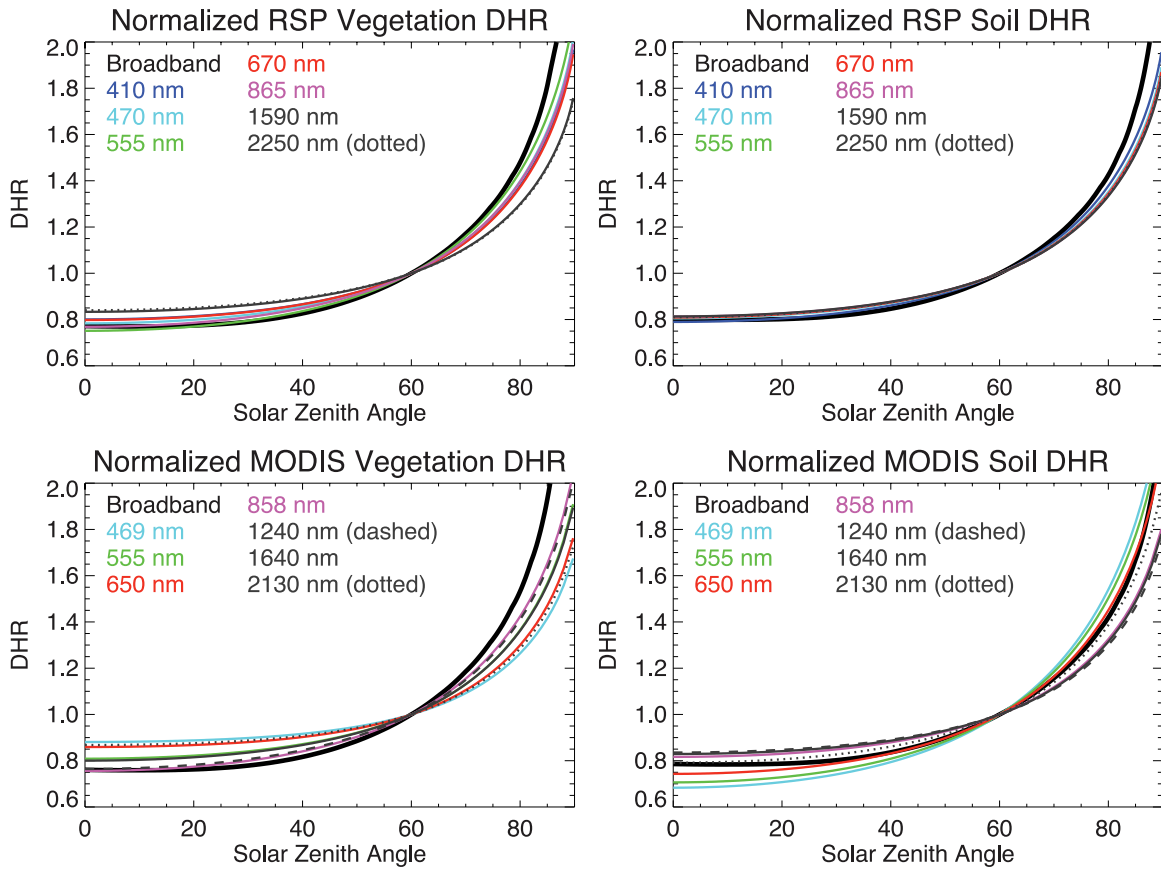


Figure 8. RSP (top) and MODIS (bottom) $DHR(\Lambda, \theta_s)$ normalized to $DHR(\Lambda, 60^\circ)$. “Vegetation” results are on the left, “soil” class results on the right.

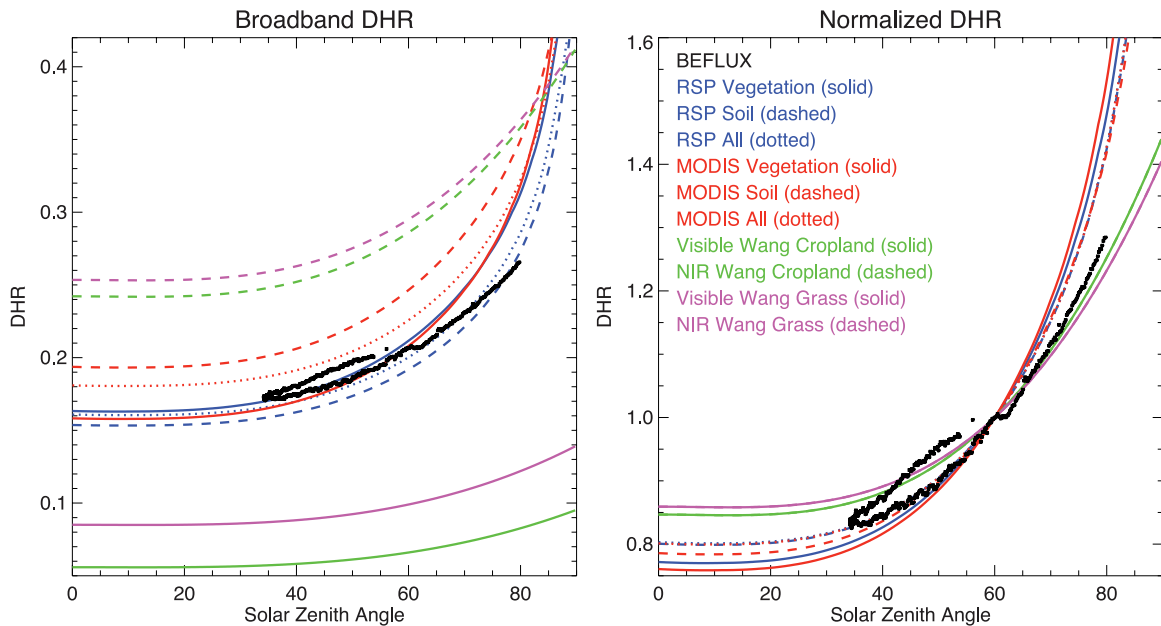


Figure 9. Comparison of broadband (left) and normalized broadband (right) DHR for BEFLUX ground radiometer data (black), RSP data (blue), MODIS data (red) and the parameterization from Wang *et al.* [2007] for “cropland” (green) and “grassland” (magenta). For RSP and MODIS, different surface types are indicated by solid lines (“vegetation”), dashed lines (“soil”) and dotted lines (“all”). Parameterizations for visible wavelengths are indicated with solid lines, and dashed lines for the NIR.

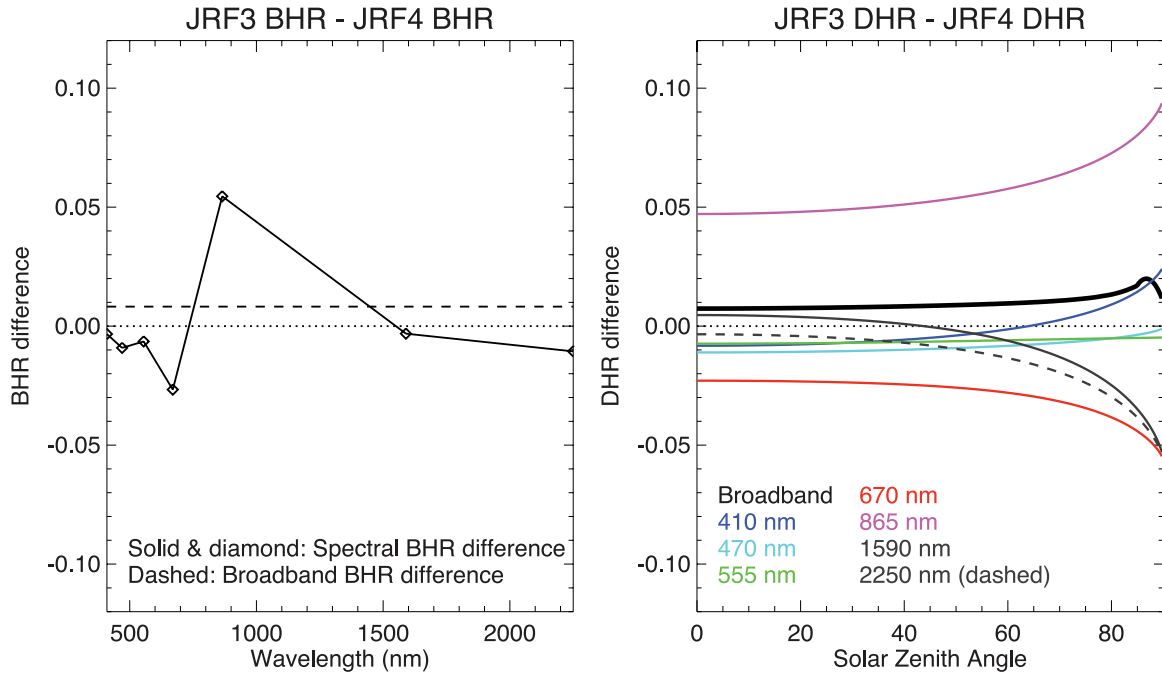


Figure 10. Differences in BHR and DHR estimated from data restricted to one flight, and thus one relative solar-view azimuth angle. The plot on the left is the difference between spectral $BHR(\lambda)$ and broadband BHR_{bb} for JRF3 and JRF4 for the “vegetation” class. The right side is the same for $DHR(\lambda, \theta_s)$ and $DHR_{bb}(\theta_s)$.

nitude of potential systematic uncertainties, such as differences due to solar azimuth angle or multiple ground-atmosphere interactions occurring in different areas adjacent to the radiometers.

[64] While it is impossible to be sure which type of surface class is best to compare with BEFLUX derived DHR (as discussed in section 3.3), it is reasonable to assume that it should be similar to one of the classes or a mixture of the two, as the small area of pasture where the BEFLUX radiometers are located is sampled in both RSP and MODIS data-sets. Indeed, this *is* the case for absolute DHR from both RSP and MODIS. The best matches are the RSP and MODIS “vegetation” classes, although other RSP classes are close as well. Of course, this comparison is limited to solar zenith angles greater than about 33° and less than about 80° , as this is the range of DHR solar zenith angles derived from BEFLUX. However, a lack of a comparison beyond this angular range should not be a significant problem when evaluating kernel based estimates of DHR and BHR . As mentioned previously, very high solar zenith angles are neither routinely measured nor energetically important for climate modeling, while the data used to estimate the Ross-Li kernel values included nadir view angles. Reciprocity of the kernel BRDF’s should therefore ensure acceptable behavior of the DHR values at small solar zenith angles. The agreement between RSP predicted and BEFLUX broadband BHR and DHR is excellent (0.0001 and on average 0.0058 for BHR and DHR , respectively, in the RSP “all” class) over the angular range from 30° to 80° . This indicates the capability of well corrected, multi-angle, narrowband results to predict the radiative balance at the surface. Although we have found larger discrepancies with

MODIS results, broadband DHR agreement is still better than 0.0042 for even the most poorly matched surface type (“soil”).

4.5. Azimuth Angle Independence

[65] RSP estimates of the BRDF are aided by the large number and range of view zenith angles of measurement available at one time. However, the results presented here represent two flights (for the “vegetation” and “all” classes) or one flight (for the “soil” class) and therefore measurements have a limited range of relative solar - view azimuth angles. Thus, while BRDF estimation is based on a well sampled meridional plane the number of such planes is very limited. While it is impossible to fully investigate the consequences of this azimuth angle measurement limitation without more data, some indication of the potential variability or uncertainty in BRDF estimates caused by this limitation can be determined by comparing results from the two flights. Figure 10 is a comparison of BRDF estimation results for JRF3 (relative solar - view azimuth, $\phi = 315^\circ$ for forward scans) and JRF4 (relative solar - view azimuth, $\phi = 156^\circ$ for forward scans) for the “vegetation” class.

[66] Comparisons of spectral BHR reveal inter-flight differences equal to or less than 0.07 for angles less than 80° . The maximum difference is in the 865nm band, which for vegetation is by far the brightest channel (see Figure 6). Broadband BHR differences are less than 0.01, less than most of the spectral BHR differences. It appears that computation of the broadband BHR removes some of the difference between the flights, which may be related to differences in the observed vegetation. Spectral DHR shows a similar pattern as BHR . Maximum differences are about

0.06 at 60° for the 865nm band, and increase with solar zenith angle. At solar zenith angles less than 80° , the flight to flight DHR_{bb} difference is about 0.01.

5. Discussion

[67] The foremost purpose of this paper is to evaluate MODIS BRDF estimates. This is done by comparing MODIS derived BHR and DHR (white and black sky albedos, in MODIS terminology) to the same values derived from an airborne sensor (RSP) and a group of ground radiometers (BEFLUX) during September in north-central Oklahoma. This is a region whose ground cover mainly included grassland and late season or recently harvested cropland. This location is important because of the presence of the SGP CF, where a host of atmospheric and radiometric instruments provide a continuous set of validation data. MODIS overestimates BHR_{bb} with respect to BEFLUX by between 0.003 and 0.042 (depending on the surface class, see Table 4). The average MODIS DHR deviation (over all angles less than 80°) from BEFLUX is 0.018, -0.002 and 0.035 for the “all”, “vegetation” and “soil” classes, respectively. Considering that BEFLUX derived DHR has differences up to 0.01 between measurements with the same solar zenith angle but at different times of day (morning and evening), we regard the MODIS DHR estimates as successful.

[68] An important component of any validation work is to identify which differences are due to the data processing necessary to perform the validation, and which represent actual instrumental differences. In this case, we recognize several processing steps that may add to or mask actual instrumental differences. Both RSP and MODIS were fit to Ross-Li BRDF models, and thus are only capable of measuring the types of BRDF that are included in those models. Another potential source of error is the need to create broadband BHR and DHR from spectral RSP and MODIS values, in order to compare to naturally broadband BEFLUX derived values. This involves interpolating between spectral bands prior to integration to broadband values, and this interpolation could miss spectral variation in the BHR or DHR that is included in the broadband values derived from BEFLUX. Finally, spatial and temporal resolution differences between satellites and point sensors on the ground are a well known source of error. We have attempted to account for these problems by separating the data into comparable classes roughly representing vegetated crops or grassland and bare (recently harvested) soil. MODIS and RSP classes are consistent with one another (see Figures 6, 7, 8 and 9), and closest with the “all” classes containing the entire dataset prior to classification. As Figure 4 shows, RSP and MODIS data-sets have a somewhat different spatial extent. So, while the classification techniques for RSP and MODIS may not be compatible, other aspects of RSP and MODIS data processing (such as spectral to broadband conversion and model fitting) produce remarkably similar results. MODIS BHR_{bb} shows a bias with respect to RSP of 0.023, -0.005 and 0.050 for the “all”, “vegetation” and “soil” classes, respectively. Average (with respect to solar zenith angles less than 80°) biases for DHR_{bb} between MODIS and RSP are 0.036, 0.006 and

0.076 for the “all”, “vegetation” and “soil” classes, respectively. $nDHR_{bb}$ has an average bias typically an order of magnitude less than absolute DHR_{bb} , indicating that differences between the instruments are primarily due to differences in the absolute magnitude of their estimates. MODIS-RSP comparisons of individual spectral bands show the same small bias for both DHR and $nDHR$.

[69] This research began as an effort to investigate some of the differences between BEFLUX radiometers and MODIS parameterizations identified by Yang [2006]. We implemented the novel DHR BEFLUX computation technique described in that paper, but did so for the much more limited time range of the ALIVE campaign. Yang [2006] compared $nDHR$ to parameterizations described by Wang *et al.* [2007] and Liang *et al.* [2005], and found the BEFLUX derived values to be larger than both parameterizations at solar zenith angles greater than 80° , and more troubling, smaller than parameterizations at angles less than 35° . Yang’s comparison utilized a third order polynomial fit because its similarity to an approximation given in Schaaf *et al.* [2002]. However, unlike the standard third-order polynomial that Yang used, the polynomial in Schaaf *et al.* [2002] is restricted to have a zero coefficient on the first-order term. Figure 11 presents the difference between these two fitting routines, where we fit both types of polynomials to our BEFLUX data. Schaaf’s polynomial fit clearly matches RSP and MODIS DHR and $nDHR$, while the Yang polynomial diverges in a similar manner to that presented in Yang [2006]. Thus, the biases that were identified in Yang [2006] are both beyond the solar zenith angle range of the reference dataset and most likely due to the choice of the data fit, rather than the data itself.

[70] The albedo parameterization presented in Wang *et al.* [2007] is also included in the comparison in Figure 9. Wang’s parameterization, described in section 3.4, is an attempt to reduce the number of parameters describing MODIS albedo from three for each band to two each for broad visible and NIR bands (which are specified for various surface types). Although these broad visible and NIR channels cannot be compared directly to broadband BEFLUX DHR , the Wang *et al.* [2007] $nDHR$ is spectrally invariant, and thus can be compared to BEFLUX derived $nDHR$. Figure 9 shows that both of the selected surfaces (grass and cropland) produce $nDHR$ with slightly shallower slopes than BEFLUX derived $nDHR$. Thus, Wang’s parameterizations show slightly smaller variation in DHR as a function of solar zenith angle compared to BEFLUX. Average (for solar zenith angle less than 80°) biases for $nDHR$ are between 0.022 and 0.028, depending on the land surface type selected for the parameterization.

6. Conclusion

[71] Generally speaking, this validation shows that there is good agreement between MODIS, RSP and BEFLUX ground radiometer derived albedos, at least for the conditions of the ALIVE experiment at the SGP CF. MODIS, which is capable of producing global BRDF estimates, produces DHR and BHR (“black-sky” and “white-sky”, albedos, respectively) that agree with aircraft measurements from RSP. RSP has a higher spatial and temporal resolution

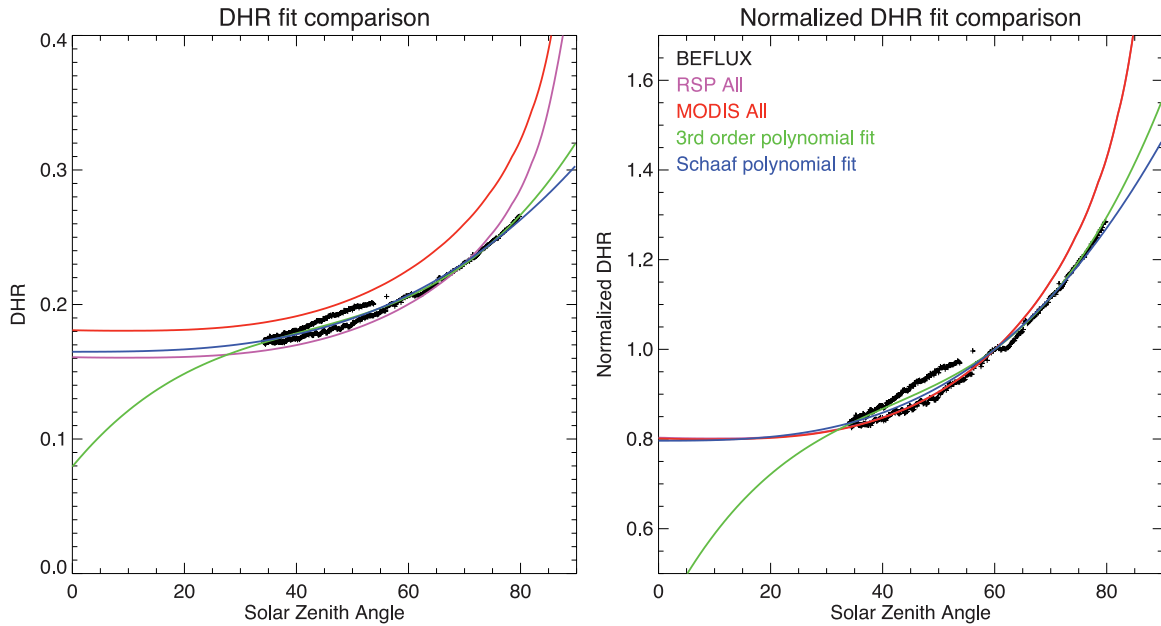


Figure 11. BEFLUX derived DHR (left) and $nDHR$ (right) and the corresponding polynomial fits to our subset of BEFLUX data, as described by Yang [2006] (green) and Schaaf *et al.* [2002] (blue). Original BEFLUX derived DHR are in black. For comparison, the “all” classes of RSP (magenta) and MODIS (red) are also included.

than MODIS, and its data are atmospherically corrected with more sophisticated algorithms, yet differences between the two are minimal. It is important to note that RSP used the same Ross-Li BRDF models employed by MODIS, so some potential instrumental differences may be masked by this similarity. However, model fitting results are robust and physically realistic. RSP and MODIS also agree well with DHR and BHR derived from the BEFLUX ground radiometers, whose methodology is quite different than the BRDF model fitting routines employed by the remote sensing instruments. A potential source of non-instrumental comparison error are the methods used to convert spectral DHR and BHR to broadband values. In our case we were required to interpolate spectral albedos and model the ground-atmosphere interaction. Previously identified differences between BEFLUX ground radiometers and MODIS were shown to be for DHR in solar zenith angles beyond the range of available comparison angles and were most likely due to the choice of the type of polynomial fit to the data, rather than instrumental effects in the data itself.

[72] This validation effort is hindered by the small quantity of data available for comparison. Cloud free, low altitude RSP measurements were limited to a single day (September 16, 2005) during the ALIVE campaign. RSP serves as an airborne prototype to the Aerosol Polarimetry Sensor (APS), due to be launched as part of the NASA Glory mission in 2008. APS is not an imaging instrument and will not be able to create global BRDF estimates like MODIS. However, the rapid angular scanning and accurate atmospheric correction of APS means that it is an ideal platform for validation of BRDF estimates from MODIS and other instruments. Pending a successful launch, Glory will join the NASA ‘A-train’ orbit, and APS will begin gathering a validation dataset much larger than what was

available for the work in this paper. The methods used here could become part of a routine BRDF remote sensing validation effort.

Appendix A: Correction for Gas Absorption

[73] Prior to assessing ground reflectance, water vapor, ozone and NO_2 absorption effects were removed from the direct solar beam. Water vapor was measured at SGP CF with a MWR, while ozone and NO_2 measurements were provided by the TOMS and SCIAMACHY orbital instruments, respectively. Absorption coefficients were computed using the spectral sensitivity of each RSP band, and applied to RSP measurements as follows:

$$I_c = I \left(e^{-M(K_{O_3}x_{O_3} + K_{NO_2}x_{NO_2}) - \alpha[wM]^\beta)} \right)^{-1} \quad (A1)$$

where I and I_c are the original and corrected radiances, respectively. K_{O_3} is the ozone absorption coefficient, x_{O_3} is the ozone quantity in centimeters per atmosphere, K_{NO_2} is the NO_2 absorption coefficient, x_{NO_2} is the quantity of NO_2 in parts per billion, w is the column water vapor, in centimeters, and parameters α and β define the optical depth due to water vapor. α , β , K_{O_3} and K_{NO_2} are given in Table A1. M is the airmass, which defines the length of the atmospheric path from the sun to the Earth surface and is well approximated for the solar zenith angles encountered here by $M = \cos(\theta_s)^{-1}$. The use of the correction procedure defined by equation (A1) is justified for ozone and nitrogen dioxide by the fact that they absorb light primarily in the stratosphere, above most atmospheric scattering. It is acceptable for water vapor because this only affects RSP bands at 1590 and 2250 nm, for which single scattering is a valid approximation of the effects of aerosols and

Table A1. Gas Absorption Parameters

Band	Wavelength	K_{O_3}	K_{NO_2}	α	β
1	410	0.000278	0.012860	0.00000	1.000000
2	469	0.010035	0.008135	0.00000	1.000000
3	555	0.096960	0.001827	0.00026	0.990068
4	670	0.044982	0.000144	0.00053	0.958742
5	864	0.002060	0.000000	0.00061	0.953774
7	1589	0.000000	0.000000	0.00251	0.645347
9	2264	0.000000	0.000000	0.01141	0.739948

molecules. Gas quantities for the day of our experiment were: 0.285 Dobson Units of Ozone, 0.74 ppb of NO₂, and precipitable water vapor between 1.237 and 1.498 cm, depending on the time of day.

Appendix B: Vegetation Indices

[74] The canonical method for assessing surface vegetation content is the Normalized Difference Vegetation Index (NDVI):

$$NDVI = \frac{L_{NIR} - L_{red}}{L_{NIR} + L_{red}} \quad (B1)$$

where L is the radiance detected by a red or near-infra red (NIR) sensor. Vegetation has a low reflectance at red wavelengths, and much higher reflectance in the NIR, while soils and other non-vegetated surfaces have much smaller spectral contrast between the red and NIR. NDVI has been used for years to assess vegetation health and cover from space, although it is important to note that it is simply an index not an actual physical parameter. However, there is the possibility that the spectral dependence of the aerosol optical properties modifies L_{NIR} and L_{red} in a manner that affects NDVI [Kaufman and Tanre, 1992]. We therefore used Kaufman and Tanre's Atmospherically Resistant Vegetation Index (ARVI) which is less sensitive to the effects of atmospheric aerosols [Kaufman and Tanre, 1992]. ARVI uses a channel at a blue wavelength in order to correct for atmospheric effects. It is defined in terms of normalized reflectances as:

$$ARVI = \frac{\rho_{NIR} - \rho_{rb}}{\rho_{NIR} + \rho_{rb}} \quad (B2)$$

$$\rho_{rb} = \rho_{red} - \gamma(\rho_{blue} - \rho_{red})$$

where γ is a parameter that depends on the aerosol type. We used a value of $\gamma = 0.9$ as suggested by Kaufman and Tanre for continental aerosols. RSP channels 2 (470 nm), 4 (670 nm) and 5 (865 nm) were used for ρ_{blue} , ρ_{red} , and ρ_{NIR} , respectively.

[75] **Acknowledgments.** The first author acknowledges support from the US National Science Foundation, through a Fellowship in the IGERT Joint Program in Applied Mathematics and Earth and Environmental Science at Columbia University at the time of the ALIVE field campaign. BEFLUX data were obtained from the Atmospheric Radiation Measurement (ARM) Program sponsored by the U.S. Department of Energy, Office of Science, Office of Biological and Environmental Research, Environmental Sciences Division. ALIVE was also funded by ARM, and RSP participation during that experiment was funded by the National Aeronautics and Space Administration (NASA). Thanks to the many who helped collect the data used in this study: Ben Hovelman was the J-31 pilot, Roy Johnson and Nicholas Truong were AATS-14 engineers, Rose Dominguez

provided J-31 Navigational and GPS data, and Warren Gore provided J-31 Meteorological data. Finally, thanks to both the anonymous reviewers.

References

- Bovensmann, H., J. Burrows, M. Buchwitz, J. Frerick, S. Noël, V. Rozanov, K. Chance, and A. Goede (1999), SCIAMACHY: Mission Objectives and Measurement Modes, *J. Atmos. Sci.*, 56(2), 127–150.
- Bruegge, C., M. Helmlinger, J. Conel, B. Gaitley, and W. Abdou (2000), PARABOLA III- A sphere-scanning radiometer for field determination of surface anisotropic reflectance functions, *Remote Sens. Rev.*, 19(1), 75–94.
- Cairns, B. (2003), Polarimetric remote sensing of aerosols, *IEEE Trans. Geosci. Remote Sens.*, 518–520.
- Cairns, B., B. Carlson, R. Ying, A. Lacis, and V. Oinas (2003), Atmospheric correction and its application to an analysis of Hyperion data, *IEEE Trans. Geosci. Remote Sens.*, 41(6), 1232–1245.
- Chahine, M. (1968), Determination of the temperature profile in an atmosphere from its outgoing radiance, *J. Opt. Soc. Am.*, 58, 1634–1637.
- Chowdhary, J., B. Cairns, and L. Travis (2002), Case studies of aerosol retrievals over the ocean from multiangle, multispectral photopolarimetric remote sensing data, *J. Atmos. Sci.*, 59(3), 383–397.
- de Haan, J., P. Bosma, and J. Hovenier (1987), The adding method for multiple scattering calculations of polarized light, *Astron. Astrophys.*, 183(2), 371–391.
- Dubovik, O., and M. King (2000), A flexible inversion algorithm for retrieval of aerosol optical properties from sun and sky radiance measurements, *J. Geophys. Res.*, 105(D16), 20,673–20,696.
- Engelsen, O., B. Pinty, M. Verstraete, and J. Martonchik (1998), Parametric surface bidirectional reflectance factor models for atmospheric radiative transfer modeling, *Geoscience and Remote Sensing Symposium Proceedings (1998)*, IGARSS'98. 1998 IEEE International, 2, 713–715.
- Gatebe, C., M. King, S. Platnick, G. Arnold, E. Vermote, and B. Schmid (2003), Airborne spectral measurements of surface-atmosphere anisotropy for several surfaces and ecosystems over southern Africa, *J. Geophys. Res.*, 108(D13), 8489, doi:10.1029/2002JD002397.
- Gonzalez, R., and R. Woods (1992), *Digital Image Processing*, Addison Wesley Publishing Company, New York.
- Hansen, J., and L. Travis (1974), Light scattering in planetary atmospheres, *Space Sci. Rev.*, 16, 527–610.
- Holben, B., Y. Kaufman, T. Eck, I. Slutsker, D. Tanre, J. Buis, A. Setzer, E. Vermote, and J. Reagan (1998), Aeronet-a federated instrument network and data archive for aerosol characterization, *Remote Sens. Environ.*, 66, 1–16.
- Hovenier, J. (1971), Multiple Scattering of Polarized Light in Planetary Atmospheres, *Astron. Astrophys.*, 13, 7.
- Jin, Y., C. Schaaf, C. Woodcock, F. Gao, X. Li, A. Strahler, W. Lucht, and S. Liang (2003), Consistency of modis surface bidirectional reflectance distribution function and albedo retrievals: 2. Validation, *J. Geophys. Res.*, 108(D5), 4159, doi:10.1029/2002JD002804.
- Kaufman, Y. J., and D. Tanre (1992), Atmospherically resistant vegetation index (arvi) for eos-modis, *IEEE Trans. Geosci. Remote Sens.*, 30, 261–270.
- Lacis, A., and J. Hansen (1974), A parameterization for the absorption of solar radiation in the earth's atmosphere, *J. Atmos. Sci.*, 31(1), 118–133.
- Li, X., and A. Strahler (1992), Geometric-optical bidirectional reflectance modeling of the discrete crown vegetation canopy: Effect of crown shape and mutual shadowing, *IEEE Trans. Geosci. Remote Sens.*, 30(2), 276–292.
- Liang, S. (2001), Narrowband to broadband conversions of land surface albedo. I: Algorithms, *Remote Sens. Environ.*, 76(2), 213–238.
- Liang, S., H. Fang, M. Chen, C. Shuey, C. Walthall, C. Daughtry, J. Morisette, C. Schaaf, and A. Strahler (2002), Validating MODIS land surface reflectance and albedo products—Methods and preliminary results, *Remote Sens. Environ.*, 83(1), 149–162.
- Liang, S., C. Shuey, A. Russ, H. Fang, M. Chen, C. Walthall, C. Daughtry, and R. Hunt Jr. (2003), Narrowband to broadband conversions of land surface albedo. II: Validation, *Remote Sens. Environ.*, 84(1), 25–41.
- Liang, X.-Z., et al. (2005), Development of land surface albedo parameterization based on moderate resolution imaging spectroradiometer (modis) data, *J. Geophys. Res.*, 110, D11107, doi:10.1029/2004JD005579.
- Long, C., D. Slater, and T. Tooman (2001), *Total Sky Imager Model 880 Status and Testing Results*, Pacific Northwest National Laboratory, Atmospheric Radiation Measurement Program, Richland, WA.
- Lucht, W., A. Hyman, A. Strahler, M. Bamsley, P. Hobson, and J. Muller (2000a), A comparison of satellite-derived spectral albedos to ground-based broadband albedo measurements modeled to satellite spatial scale for a semidesert landscape, *Remote Sens. Environ.*, 74(1), 85–98.
- Lucht, W., C. Schaaf, and A. Strahler (2000b), An algorithm for the retrieval of albedo from space using semiempirical brdf models, *IEEE Trans. Geosci. Remote Sens.*, 38(2), 977–998.

- Luo, Y., A. Trishchenko, R. Latifovic, and Z. Li (2003), Surface bi-directional reflectance properties over the arm sgp area from satellite multi-platform observations, in *Proceedings of the Thirteenth Atmospheric Radiation Measurement (ARM) Science Team Meeting*, edited by D. Carrothers, pp. 1–12, Department of Energy, Richland, Wash.
- Luo, Y., A. P. Trishchenko, R. Latifovic, and Z. Li (2005), Surface bidirectional reflectance and albedo properties derived using a land cover based approach with moderate resolution imaging spectroradiometer observations, *J. Geophys. Res.*, **110**, D01106, doi:10.1029/2004JD004741.
- Martonchik, J., D. Diner, K. Crean, and M. Bull (2002), Regional aerosol retrieval results from misr, *IEEE Trans. Geosci. Remote Sens.*, **40**(7), 1520–1532.
- McPeters, R., and G. Center (1998), Earth Probe Total Ozone Mapping Spectrometer (TOMS) Data Product User's Guide, NASA TP-1998-206895, National Aeronautics and Space Administration, Goddard Space Flight Center; National Technical Information Service.
- Mishchenko, M., B. Cairns, J. Hansen, L. Travis, R. Burg, Y. Kaufman, J. Vanderlei Martins, and E. Shettle (2004), Monitoring of aerosol forcing of climate from space: Analysis of measurement requirements, *J. Quant. Spectrosc. Radiat. Transfer*, **88**(1–3), 149–161.
- Mishchenko, M., I. Geogdzhayev, B. Cairns, B. Carlson, J. Chowdhary, A. Lacis, L. Liu, W. Rossow, and L. Travis (2007a), Past, present, and future of global aerosol climatologies derived from satellite observations: A perspective, *J. Quant. Spectrosc. Radiat. Transfer*, **106**, 325–347.
- Mishchenko, M., B. Cairns, G. Kopp, C. F. Schueler, B. A. Fafaul, J. E. Hansen, R. J. Hooker, T. Itchkawich, H. B. Maring, and L. D. Travis (2007b), Accurate monitoring of terrestrial aerosols and total solar irradiance: Introducing the Glory mission, *Bull. Amer. Meteorol.*, **88**.
- Morris, V. (2006), Microwave radiometer (mwr) handbook, *Tech. Rep. ARM TR-016*, U.S. Department of Energy, Argonne, IL.
- Myhre, G., and A. Myhre (2003), Uncertainties in radiative forcing due to surface albedo changes caused by land-use changes, *J. Clim.*, **16**(10), 1511–1524.
- Nicodemus, F. E., J. C. Richmond, J. J. Hsia, I. W. Ginsberg, and T. Limperis (1977), *Geometrical Considerations and Nomenclature for Reflectance*, US Dept. of Commerce, National Bureau of Standards, Supt. of Docs., US Govt. Print. Off., Washington, D. C.
- Pinty, B., A. Lattanzio, J. Martonchik, M. Verstraete, N. Gobron, M. Taberner, J. Widlowski, R. Dickinson, and Y. Govaerts (2005), Coupling Diffuse Sky Radiation and Surface Albedo, *J. Atmos. Sci.*, **62**(7), 2580–2591.
- Ross, J. (1981), *The Radiation Regime and Architecture of Plant Stands*, W. Junk, Norwell, Mass.
- Roujean, J., M. Leroy, and P. Deschanps (1992), A bidirectional reflectance model of the Earth's surface for the correction of remote sensing data, *J. Geophys. Res.*, **97**(D18), 20,455–20,468.
- Salomon, J., C. Schaaf, A. Strahler, F. Gao, and Y. Jin (2006), Validation of the MODIS bidirectional reflectance distribution function and albedo retrievals using combined observations from the aqua and terra platforms, *IEEE Trans. Geosci. Remote Sens.*, **44**(6), 1555–1565.
- Schaaf, C., A. Strahler, M. Roman, J. Salomon, and J. Hodges (2006), Assessment of albedo derived from the moderate-resolution imaging spectroradiometer at the southern great plains site, in *Proceedings of the Sixteenth ARM Science Team Meeting*, pp. 1–2, Department of Energy Atmospheric Radiation Measurement Program, Albuquerque, NM.
- Schaaf, C., F. Gao, A. H. Strahler, W. Lucht, X. Li, T. Tsang, N. C. Strugnell, X. Zhang, Y. Jin, and J. P. Muller (2002), First operational BRDF, albedo nadir reflectance products from MODIS, *Remote Sens. Environ.*, **83**(1), 135–148.
- Schaeppman-Strub, G., M. Schaeppman, T. Painter, S. Dangel, and J. Martonchik (2006), Reflectance quantities in optical remote sensing: Definitions and case studies, *Remote Sens. Environ.*, **103**(1), 27–42.
- Schmid, B., et al. (2006), How well do state-of-the-art techniques measuring the vertical profile of tropospheric aerosol extinction compare, *J. Geophys. Res.*, **111**, D05507, doi:10.1029/2005JD005837.
- Shi, Y., and C. Long (2002), *Best Estimate Radiation Flux Value-added Procedure: Algorithm Operational Details and Explanations*, ARM TR-008, Pacific Northwest National Laboratory, Richland, WA.
- Strahler, A., W. Lucht, C. Schaaf, T. Tsang, F. Gao, X. Li, J. Muller, P. Lewis, and M. Barnsley (1999), MODIS BRDF/Albedo Product: Algorithm Theoretical Basis Document Version 5.0, Tech. rep., National Aeronautics and Space Administration.
- Twomey, S. (1977), The Influence of Pollution on the Shortwave Albedo of Clouds, *J. Atmos. Sci.*, **34**(7), 1149–1152.
- Wang, Z., X. Zeng, and M. Barlage (2007), Moderate resolution imaging spectroradiometer bidirectional reflectance distribution function-based albedo parameterization for weather and climate models, *J. Geophys. Res.*, **112**, D02103, doi:10.1029/2005JD006736.
- Wanner, W., X. Li, and A. Strahler (1995), On the derivation of kernel-driven models of bidirectional reflectance, *J. Geophys. Res.*, **100**(D10), 21,077–21,090.
- Yang, F. (2006), Parameterizing the dependence of surface albedo on solar zenith angle using atmospheric radiation measurement observations, in *Proceedings of the Sixteenth ARM Science Team Meeting Proceedings*, Albuquerque, NM.

B. Cairns and K. D. Knobelspiesse, Department of Applied Physics and Applied Mathematics, Columbia University, NASA GISS, 2880 Broadway, New York, NY 10025, USA. (kdk2103@columbia.edu)

M. O. Román and C. B. Schaaf, Department of Geography and Environment, Center for Remote Sensing, Boston University, 675 Commonwealth Avenue STO-457, Boston, MA 02215, USA.

B. Schmid, Atmospheric Science and Global Change Division, Pacific Northwest National Laboratory, 902 Battelle Boulevard, P.O. Box 999, MSIN K9-24, Richland, WA 99352, USA.